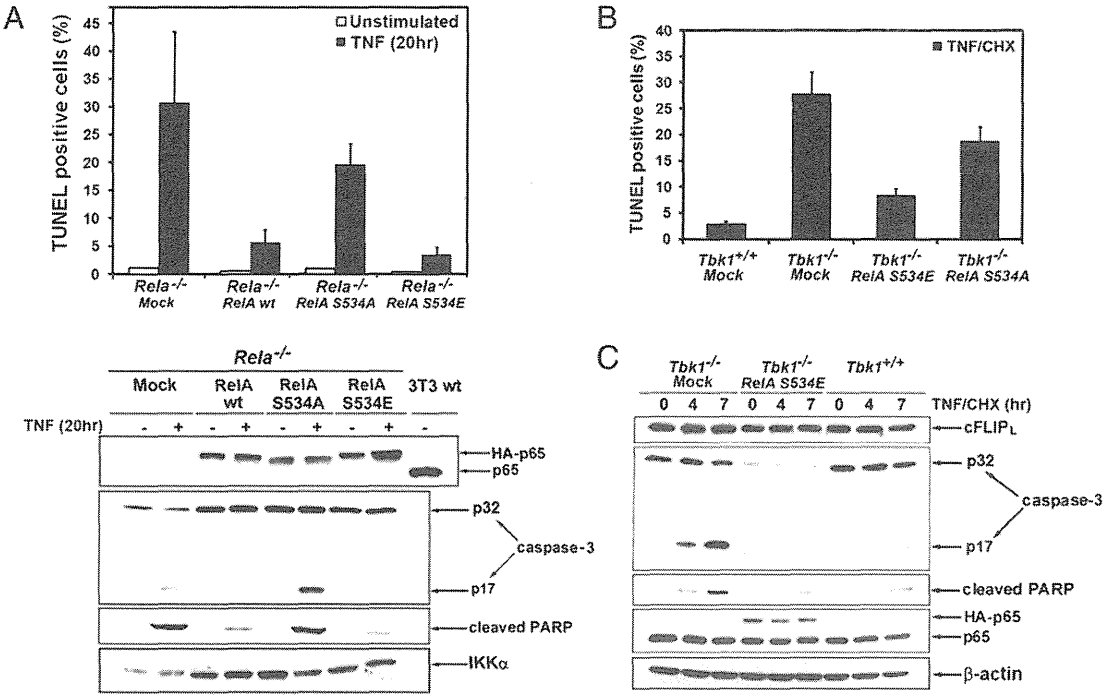

Fig. 2. Phospho-RelA protects MEFs from TNF-induced apoptosis. (*A*) *Rela*$^{-/-}$ MEFs infected with an empty retrovirus (mock) or retroviruses expressing HA-tagged wt RelA, RelA(S534A), or RelA(S534E) were left unstimulated or were treated with TNF (20 h). Apoptotic cells were detected by TUNEL staining. Represented are averages ± SD of three separate experiments. Cell lysates were analyzed for caspase-3 activation, PARP cleavage, and RelA expression by immunoblotting. (*B*) *Tbk1*$^{-/-}$ MEFs expressing RelA(S534A) or RelA(S534E) were treated for 3 h with TNF in the presence of CHX. Apoptotic cells were detected by TUNEL assay and quantified as described earlier. (*C*) Lysates were prepared from cells in *B* that were stimulated with TNF plus CHX for the indicated times. Caspase-3 activation and protein expression were determined by immunoblotting as in *A*.

subunits indicated that a functional IKK complex was also required for TNF-induced RelA phosphorylation (Fig. S5*A*). These results are consistent with our early suggestion that TBK1 stimulates NF-κB activity through the canonical IKK complex (9). By using an established peptide mapping strategy (19), the TNF-inducible phosphorylation sites were localized to a 4.6-kDa CNBr peptide located in the C-terminal transactivation domain of RelA (Fig. S4 *B* and *C*). The major TNF-inducible phosphorylation site was identified as Ser^{534} of mouse RelA (corresponding to Ser^{536} of human RelA; Fig. S4*D*). Reduced Ser^{534} phosphorylation in *Tbk1*$^{-/-}$ MEFs was confirmed by immunoblotting performed with phospho-specific RelA antibody (Fig. 1*F*). RelA Ser^{534} phosphorylation was also impaired in cells defective in both IKK catalytic subunits (Fig. S5*B*). Ser^{534} phosphorylation took place in the cytosol, as it was dramatically reduced in *IκBα*$^{-/-}$ MEFs, in which most of RelA is constitutively nuclear (Fig. S5*C*).

Ser^{534} Phosphorylation Regulates RelA Antiapoptotic Function. To examine whether phosphorylation of RelA at Ser^{534} was required to protect MEFs from TNF-induced apoptosis, a retroviral vector was used to stably express WT RelA, RelA(S534A), or a phospho-mimic RelA(S534E) mutant in *Rela*$^{-/-}$ MEFs. Expression levels were similar to that of endogenous RelA in WT MEFs (Fig. 2*A*), and all the expressed proteins underwent nuclear translocation. Whereas WT RelA and RelA(S534E) protected *Rela*$^{-/-}$ MEFs from TNF-induced apoptosis, expression of RelA(S534A) provided little protection (Fig. 2*A*). Similar results were obtained when caspase-3 activation and cleavage of PARP were examined: WT RelA and RelA(S534E) prevented caspase-3 activation, whereas RelA(S534A) did not (Fig. 2*A*). Expression of RelA(S534E) but not RelA(S534A) also prevented apoptosis (Fig. 2*B*), PARP cleavage, and caspase-3 activation (Fig. 2*C*) in *Tbk1*$^{-/-}$ MEFs. Surprisingly, the amount of procaspase-3 was dramatically reduced in *Tbk1*$^{-/-}$ MEFs expressing RelA(S534E) (Fig. 2*C*). This reduction in procaspase-3 protein amount appeared to be specific, as other proteins such as cFLIP$_L$ (Fig. 2*C*) and XIAP (Fig. 3*G*) were not affected.

TBK1 Controls TNF-Induced Expression of Survival Gene *Pai-2/serpinB2*. Genes that mediate the survival function of TBK1 were identified by microarray analysis of RNAs isolated from resting and TNF-stimulated WT and *Tbk1*$^{-/-}$ MEFs. Selected data were validated by quantitative real-time PCR (qRT-PCR). Induction of most previously described (20) NF-κB–dependent genes was not affected by TBK1 deficiency (Fig. S6). As expected, induction of genes that require activation of IFN regulatory factors in addition to NF-κB, such as *IP-10*, *Rantes*, or *Irf9* was impaired in TNF-stimulated *Tbk1*$^{-/-}$ MEFs (Fig. 3*A* and Fig. S6). Among well established antiapoptotic genes, induction of *c-Iap-1*, *c-Iap-2*, *Xiap*, and *BclX$_L$* was observed in *Tbk1*$^{-/-}$ MEFs, whereas *c-Flip* expression was constitutive and not TNF-inducible in MEFs (Fig. S6). Further examination of less studied NF-κB target genes with a documented survival function identified *Pai-2/serpinb2*, a gene encoding PAI-2, a serine protease inhibitor previously shown to inhibit TNF-induced apoptosis in cancer cells (21, 22), as a potential candidate (Fig. 3*A*). Both basal (Fig. 3*A*, *Inset*) and TNF-induced expressions of *Pai-2* were dramatically reduced in *Tbk1*$^{-/-}$ MEFs (Fig. 3*A*). However, *Pai-2* expression was restored in *Tbk1*$^{-/-}$ MEFs upon expression of RelA(S534E), whereas *IP-10* induction remained defective (Fig. 3*B*). Induction of other NF-κB–dependent genes such as *IκBα* and *iNos* was not affected (Fig. 3*B*). Reconstitution of *Tbk1*$^{-/-}$ MEFs with RelA(S534E) also increased PAI-2 protein expression (Fig. 3*C*).

The antiapoptotic function of ectopic PAI-2 reintroduced into *Tbk1*$^{-/-}$ MEFs was examined by retroviral transduction. Recon-

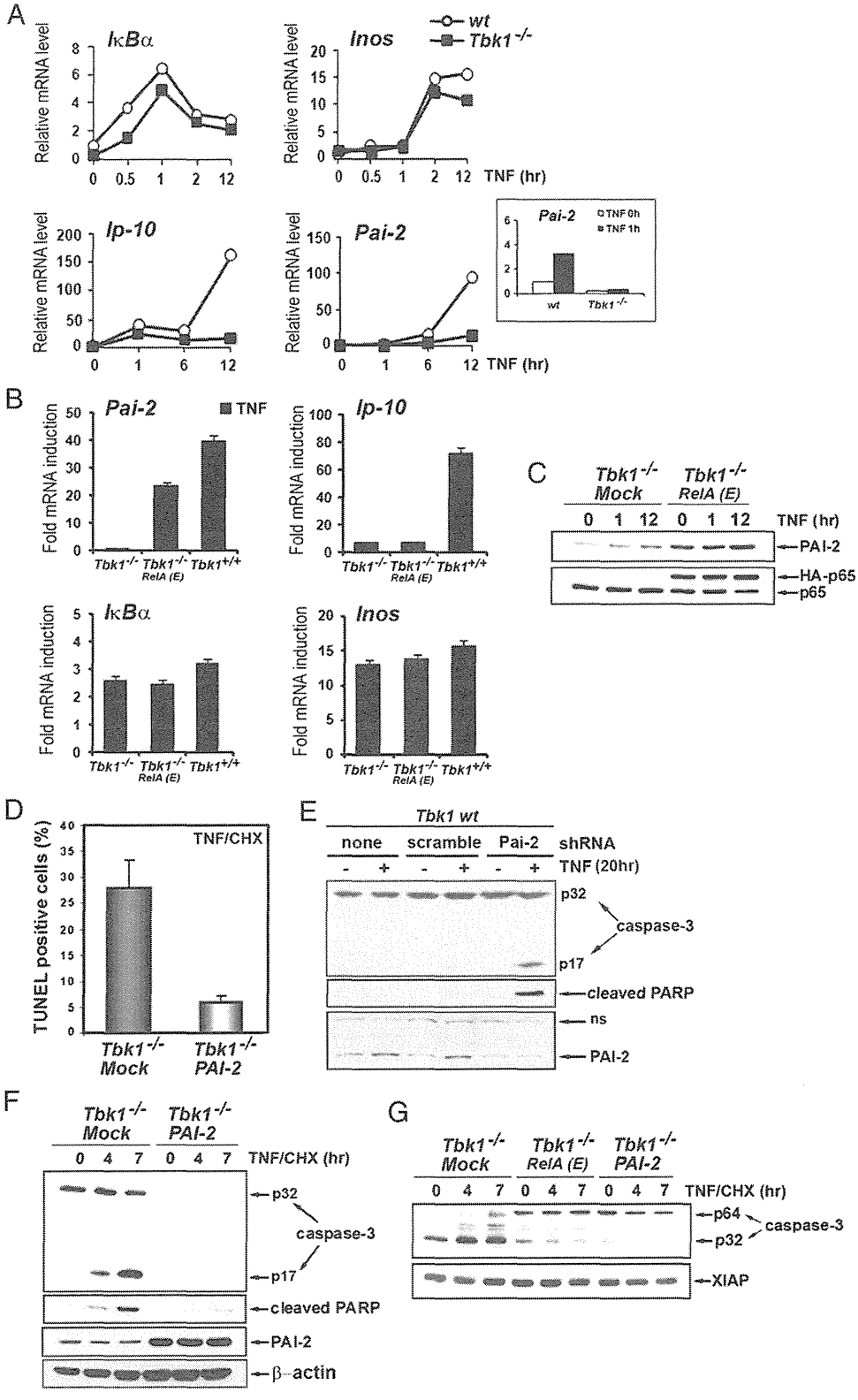

Fig. 3. TBK-1 controls NF-κB–dependent expression of the survival factor PAI-2. (*A*) Induction of NF-κB target genes was determined by qRT-PCR amplification of mRNAs prepared from WT and *Tbk1*$^{-/-}$ MEFs that were stimulated with TNF for the indicated times. *Inset*: Short time course (0 and 1 h) of *Pai-2* mRNA induction in both cell types. (*B*) Relative mRNA induction was analyzed by qRT-PCR amplification of RNAs prepared from WT (*Tbk1*$^{+/+}$), *Tbk1*$^{-/-}$, and *Tbk1*$^{-/-}$ MEFs expressing RelA(S534E), depicted as RelA(E) that were stimulated with TNF for 2 h (*IκBα*), 6 h (*Pai-2* and *Inos*), or 14 h (*Ip10*). (*C*) Expression of endogenous PAI-2 and RelA was examined by immunoblotting in extracts prepared from cells that were stimulated with TNF for the indicated times. (*D*) Apoptotic cell death, determined by TUNEL assay as described earlier, was quantified in *Tbk1*$^{-/-}$ MEFs and in cells stably expressing PAI-2 that were stimulated for 3 h with TNF in the presence of CHX. (*E*) WT MEFs expressing a *Pai-2* shRNA or a scrambled shRNA were treated with TNF for 20 h. Caspase-3 activation, PARP cleavage, and protein expression were determined by immunoblotting. (*F* and *G*) Caspase-3 activation, PARP cleavage, and protein expression were determined by immunoblotting in extracts prepared from the indicated cells that were stimulated with TNF in the presence of CHX for the indicated times.

stituted cells were protected from TNF-induced apoptosis (Fig. 3*D*) or activation of caspase-3 (Fig. 3*F*). By contrast, down-regulation of *Pai-2* expression by stably expressing a *Pai-2*-specific shRNA, but not a scrambled shRNA, potentiated TNF-induced caspase-3 activation and apoptosis in WT MEFs (Fig. 3*E*). Similarly to what was observed in $Tbk1^{-/-}$ MEFs expressing RelA(S534E), the amount of procaspase-3 was dramatically reduced in $Tbk1^{-/-}$ MEFs expressing PAI-2, and a slow-migrating form of procaspase-3 with an apparent molecular weight of 64 kDa (depicted as p64) was observed in $Tbk1^{-/-}$ MEFs expressing either RelA (S534E) or PAI-2 (Fig. 3*G*). A similar slow-migrating caspase-3 isoform was previously described as a cross-linked procaspase-3 in thapsigargin-treated HCT116 cancer cells and in tumor cells exposed to hypoxia (23, 24). In both cases, caspase-3 cross-linking into nonfunctional dimers or multimers is mediated by TG2, a multifunctional enzyme that induces posttranslational protein modifications by transamidation (25). TG2 was reported to have antiapoptotic function not only in vitro (23, 24) but also in vivo, as TG2-deficient mice show increased sensitivity to apoptosis induced by activation of the CD95/Fas receptor (26), a molecule related to TNFR1.

TG2 Is a TBK1-Regulated Antiapoptotic Factor. Endogenous TG2 activity was analyzed in WT and $Tbk1^{-/-}$ MEFs stimulated with TNF by examining incorporation of biotinylated pentylamines into cellular proteins (27). TNF induced transamidation in WT MEFs but not in $Tbk1^{-/-}$ MEFs (Fig. 4*A*). TNF also failed to stimulate *Tg2* gene expression in $Tbk1^{-/-}$ MEFs, whereas expression of *Tg1* was somehow increased in these cells (Fig. 4*B*). TG2 protein could hardly be detected in MEFs because of the poor quality of available antibodies combined with its very low level of expression. However, we could observe that basal and TNF-induced endogenous TG2 protein amounts were increased in $Tbk1^{-/-}$ MEFs expressing RelA(S534E) (Fig. 4*C*, *Upper*). Interestingly, basal TG2 expression was also increased in $Tbk1^{-/-}$ MEFs constitutively expressing PAI-2, suggesting that PAI-2 might stabilize TG2 (Fig. 4*C*, *Lower*). Similarly, MEFs treated with the proteasome inhibitor MG132 contained more TG2 protein (Fig. S7*A*), suggesting the existence of a tight posttranslational control that down-regulates TG2 protein expression. Consistent with PAI-2's involvement in stabilization of TG2, an interaction between PAI-2 and TG2 was observed by coimmunoprecipitation in MEFs expressing HA-PAI-2 and human TG2 (Fig. 4*D*). We next examined whether the activity responsible for cross-linking of procaspase-3 was associated with PAI-2. An in vitro transamidation assay was performed with PAI-2 immunoprecipitates from $Tbk1^{-/-}$ MEFs stably expressing untagged PAI-2 that were left untreated or were stimulated with TNF, and recombinant HA-procaspase-3 generated by in vitro translation was used as a substrate. Caspase-3 cross-linking activity was present in PAI-2 immunoprecipitates but not in control immunoprecipitates, and it was strongly elevated in TNF stimulated cells (Fig. S7*B*). Similarly, TG2 immunoprecipitated from MEFs expressing TG2 and PAI-2 showed inducible transamidation activity toward procaspase-3 (Fig. 4*E*). Assays performed by using recombinant PAI-2 or TG2 further confirmed that the transamidating activity was carried out by TG2 and not by PAI-2 (Fig. 4*E*, *Right*).

We next examined if the protective effect of PAI-2 and TG2 was indeed mediated through inhibition of caspase-3 without affecting alternative (i.e., mitochondrial-mediated) pathways. A slight increase in BID cleavage after stimulation with TNF and CHX was observed in $Tbk1^{-/-}$ MEFs relative to WT cells (Fig. S8*A*). Expression of PAI-2 in these cells was unable to prevent BID cleavage (Fig. S8*B*), suggesting that PAI-2 is not a bona fide antiapoptotic factor. We also analyzed TNF-induced apoptosis in cells defective in caspase-3. In agreement with previous studies (28, 29), we found that caspase-3–deficient ($Casp3^{-/-}$) MEFs were highly resistant to TNF-induced apoptosis (Fig. S8*C*), highlighting that the absence of caspase-3 does not generate a compensatory cell death pathway (e.g., TNF-induced BID cleavage) in MEFs and that caspase-3 is indeed critical to mediate the TNF response in these cells. Taken together, these experiments clearly indicated that PAI-2 and TG-2 act specifically on TNF-induced, caspase-3–dependent apoptosis.

To examine the antiapoptotic function of TG2, we first used the irreversible TG2 inhibitor KCC009 (30). As shown in Fig. 4*F*, treatment with KCC009 strongly potentiated TNF-induced caspase-3 activation and apoptosis in WT MEFs. To further confirm the antiapoptotic function of TG2, primary MEFs derived from $Tg2^{+/+}$ and $Tg2^{-/-}$ littermate embryos (31) were examined for their sensitivity to TNF-induced apoptosis. Apoptosis (PARP cleavage) and caspase-3 activation were detected by immunoblotting (Fig. 4*G*). Caspase-3 activation was observed in $Tg2^{-/-}$ MEFs treated with TNF without the need for inhibition of de novo protein synthesis, indicating that these cells have an intrinsic defect in the antiapoptotic response to TNF. The extent of cell death was quantified by staining with propidium iodide (PI) (Fig. 4*H*) and FACS analysis after annexin V and PI staining confirmed that $Tg2^{-/-}$ MEFs showed increased susceptibility to TNF-induced apoptosis (Fig. S9).

TG2 Is Essential for Prevention of TNF-Dependent Liver Injury. To assess the antiapoptotic function of TG2 in vivo, we used two models of TNF-induced liver injury in mice. WT and $Tg2^{-/-}$ mice were first injected intraperitoneally with TNF and actinomycin D (Act D). $Tg2^{-/-}$ mice showed clear signs of liver failure such as elevated serum aspartate aminotransferase (AST) and alanine aminotransferase (ALT) levels (Fig. 5*A*), massive infiltration with neutrophils, and presence of numerous apoptotic bodies (Fig. 5*B*). The presence of a high amount of TUNEL-positive cells at the injury sites indicated that cell death mainly occurred through apoptosis (Fig. 5*B*). Caspase-3 activation was also observed in liver extracts from $Tg2^{-/-}$ mice injected with TNF and Act D (Fig. 5*C*). To rule out that apoptosis occurred in endothelial cells, staining with anti-CD31 (PECAM-1), which detects endothelial cells, was performed on sections consecutive to those used for histological evaluation and TUNEL assays. The absence of TUNEL-positive cells in the CD31-positive population, combined with histological evaluation, indicated that hepatocytes were the major cell type undergoing apoptosis in TNF/Act D-challenged $Tg2^{-/-}$ mice (Fig. 5*B*). $Tg2^{+/+}$ mice also experienced liver damage, but the response was much weaker than in $Tg2^{-/-}$ mice (Fig. 5*A*) and no caspase-3 activation could be detected (Fig. 5*C*). Thus, $Tg2^{-/-}$ mice are more susceptible to TNF-induced liver injury than WT mice. $Tg2^{-/-}$ mice were also highly sensitive to T cell-mediated liver injury induced by i.v. injection of Con A, which is TNF-dependent. Liver damage indicated by ALT release was present in both genotypes but was more severe in $Tg2^{-/-}$ mice (Fig. 5*D*). Massive hepatocyte cell death detected by TUNEL staining was observed in $Tg2^{-/-}$ liver sections 8 h after Con A injection (Fig. 5*E*), and caspase-3 activation indicated that cell death in $Tg2^{-/-}$ mice occurred through apoptosis (Fig. 5*F*). Liver destruction was clearly visible 24 h after Con A injection in $Tg2^{-/-}$ mice, and the apoptotic cell remnants could no longer be detected by TUNEL reaction. Only few apoptotic hepatocytes were found in liver sections from $Tg2^{+/+}$ mice (Fig. 5*E*), and caspase-3 activation was not observed (Fig. 5*F*). These data strongly support the physiological relevance of TG2 as an inhibitor of TNF-induced apoptosis.

Discussion

The role of TBK1 in mediating the innate immune response to viruses and dsDNA through induction of type I IFN is well documented. By contrast, the role of TBK1 in IKK–NF-κB signaling has been debated, because of the observation that, al-

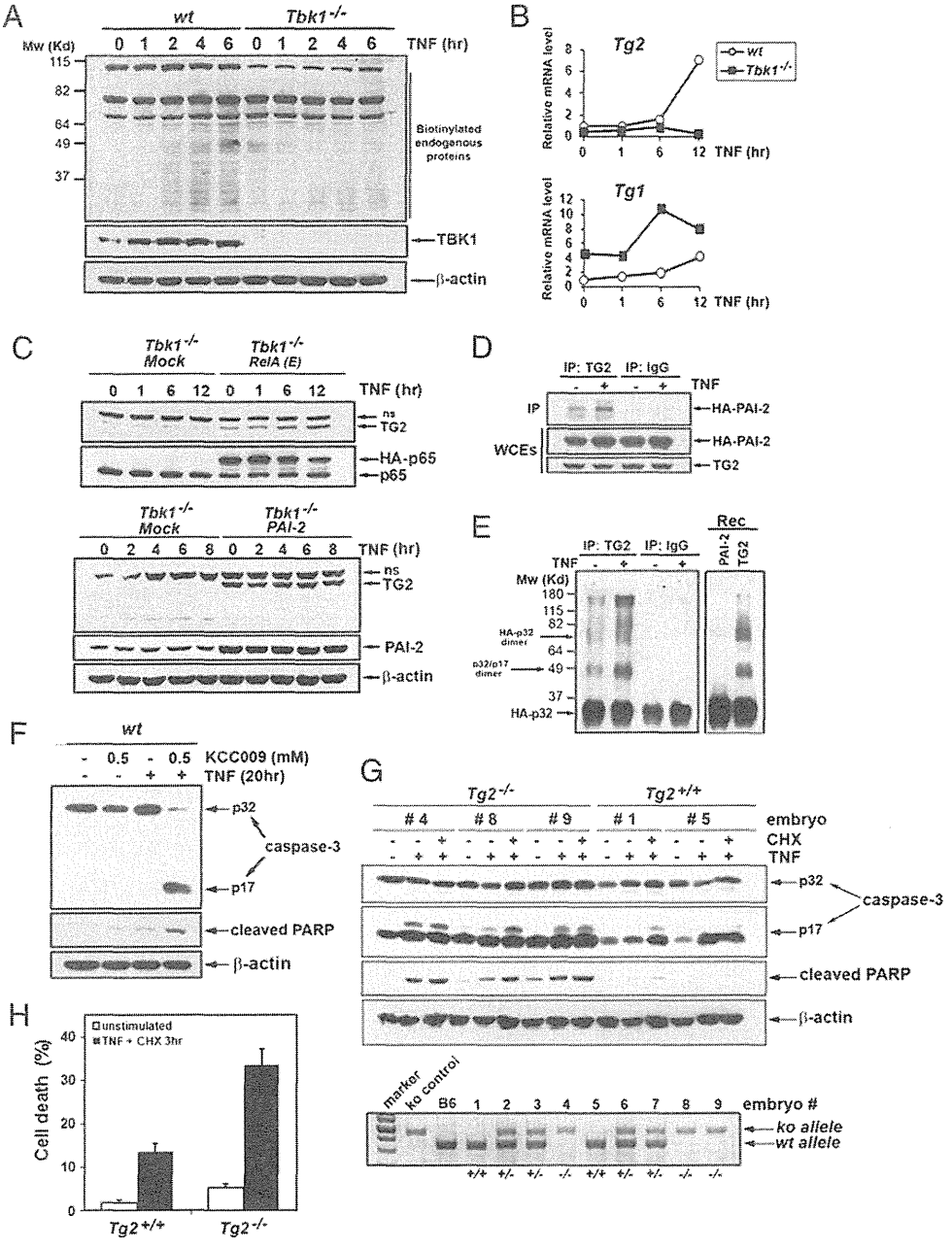

Fig. 4. TG2 is a TBK1-dependent antiapoptotic factor. (*A*) In vivo transamidation activity was determined in WT and *Tbk1*$^{-/-}$ MEFs metabolically labeled with BP and stimulated with TNF for the indicated times. Cell extracts were prepared, and biotin-conjugated proteins were detected by immunoblotting using anti–streptavidin-HRP (Pierce). (*B*) Induction of *Tg* gene expression was determined by qRT-PCR analysis of mRNAs from WT and *Tbk1*$^{-/-}$ MEFs stimulated with TNF for the indicated times. (*C*) Endogenous TG2 protein amounts were determined by immunoblotting in extracts from *Tbk1*$^{-/-}$ MEFs expressing RelA(E) (*Upper*), PAI-2 (*Lower*), or an "empty" retrovirus (mock) and treated with TNF for the indicated times (ns, nonspecific). (*D*) Coimmunoprecipitation of PAI-2 with TG2 was examined in MEFs stably expressing HA-PAI-2 and human TG2 that were left untreated or were stimulated with TNF for 8 h. Control immunoprecipitations were performed with nonimmune IgGs. (*E*) In vitro transamidation assay was performed with TG2 or control immunoprecipitates prepared from untreated or TNF-stimulated *Tbk1*$^{-/-}$ MEFs expressing TG2 and untagged PAI-2 or with recombinant proteins (rec) using HA-procaspase-3 as a substrate. (*F*) Wt MEFs were treated with TNF (20 h) with or without the transglutaminase-specific inhibitor KCC009 (0.5 mM). Caspase-3 activation, PARP cleavage, and protein expression were determined by immunoblotting. (*G*) WT and *Tg2*$^{-/-}$ primary MEFs prepared from littermate embryos were left untreated or treated with TNF alone (20 h) or TNF plus CHX (6 h). Caspase-3 activation and apoptosis were determined as detailed earlier. Genotyping (*Lower*) was performed by PCR amplification as described (31). (*H*) The extent of cell death in WT and *Tg2*$^{-/-}$ MEFs that were stimulated for 3 h with TNF plus CHX was quantified by staining with PI.

though TBK1 affects NF-κB target gene expression, it is not required for activation of NF-κB DNA binding (11). Early studies found TBK1 to form a complex with the adaptor molecules TRAF2 and TANK (8), which mediate assembly of signaling complexes at the intracellular tails of cytokine receptors (32). Indeed, TBK1 is recruited to TNFR1 upon TNF binding (10) and interacts with IKKγ/Nemo, the regulatory subunit of IKK (33, 34). We reported that TBK1 activates NF-κB through phosphorylation-mediated activation of the IKK complex (9). Consistent with a role for TBK1 in NF-κB signaling, *Tbk1*$^{-/-}$

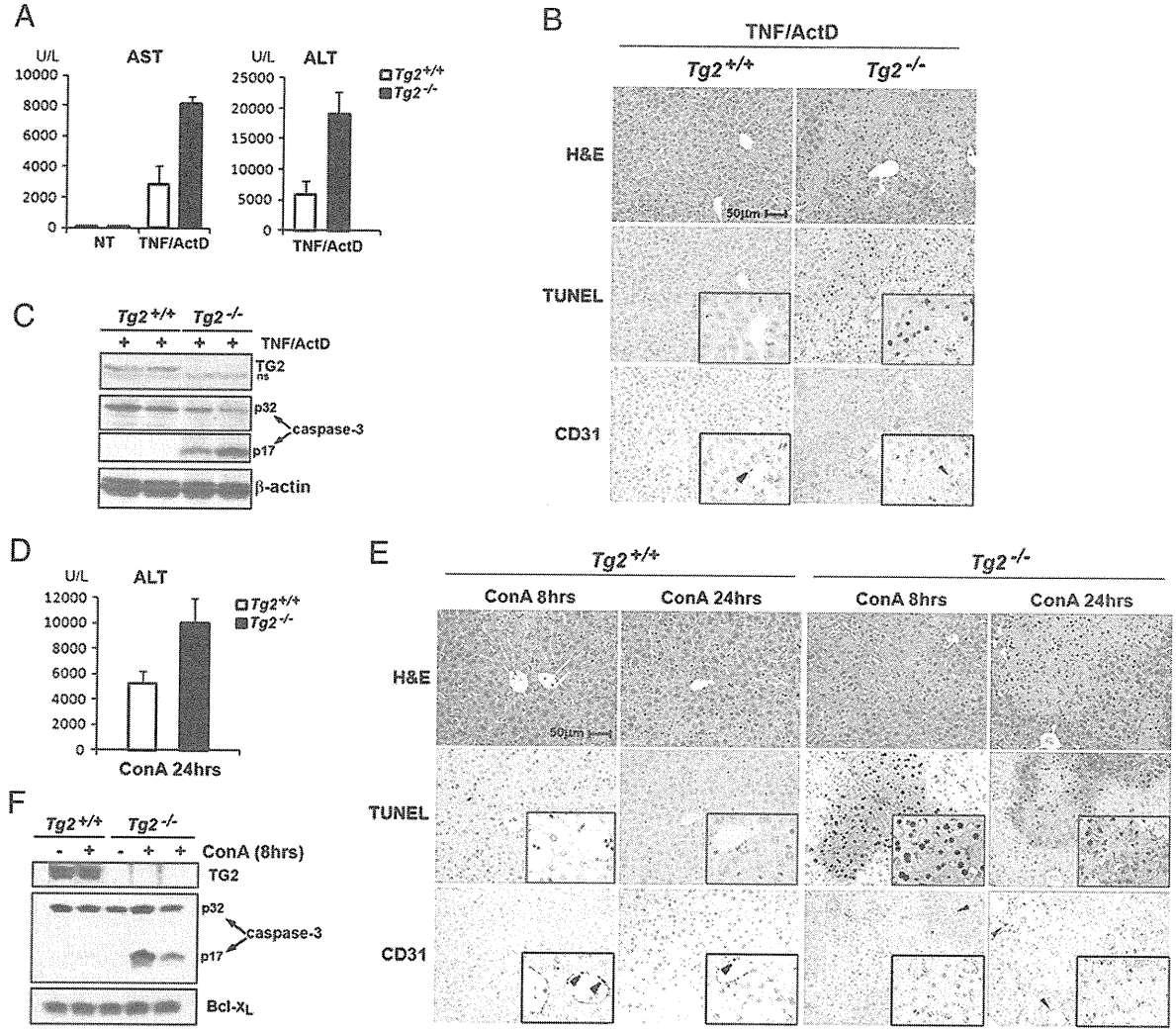

Fig. 5. TG2 protects mice from TNF-dependent liver apoptosis. (*A–C*) WT and $Tg2^{-/-}$ mice were injected with TNF and ActD and analyzed 16 h later. (*A*) Serum AST and ALT levels were determined in untreated mice (NT) or mice treated with TNF and Act D. Data are averages ± SD ($n = 3$). (*B*) Histological analysis (H&E staining), TUNEL staining, and anti-CD31 immunostaining were performed on sequential liver sections of WT and $Tg2^{-/-}$ mice 16 h after TNF and Act D injection. *Insets*: Higher magnification of a selected area. Arrowheads show vascular endothelial cells (CD31-positive), which are TUNEL-negative. CD31 immunostaining in $Tg2^{-/-}$ liver sections displayed some nonspecific background staining as a result of the presence of cell debris. (*C*) Caspase-3 activation was determined by immunoblot analysis of liver protein extracts prepared 16 h after TNF and Act D injection. (*D–F*) The same analyses were performed on WT and $Tg2^{-/-}$ at 8 h (*E* and *F*) or 24 h (*D* and *E*) after injection of Con A (35 mg/kg). (*D*) Serum AST and ALT levels measured after Con A injection. Data are averages ± SD ($n = 2$). (*E*) Histological analysis, TUNEL assays, and anti-CD31 staining were performed on sequential liver sections of WT and $Tg2^{-/-}$ mice at 8 h or 24 h after injection of Con A. *Insets*: Higher magnification of a selected area. TUNEL-positive cells (nuclear staining) in $Tg2^{-/-}$ liver sections are CD31-negative and represent apoptotic hepatocytes. Twenty-four hours of treatment with Con A induced massive liver degeneration in $Tg2^{-/-}$ mice, and dead cells were no longer detectable by TUNEL staining. Arrowheads point to vascular endothelial cells (CD31-positive cells), which are TUNEL-negative. (*F*) Liver extracts prepared from WT and $Tg2^{-/-}$ mice challenged with Con A (8 h) or PBS solution were analyzed for caspase-3 activation.

mice die during embryonic development from massive liver apoptosis and, like $Rela^{-/-}$, $Ikk\beta^{-/-}$, and $Ikk\gamma^{-/-}$ mice, they can be rescued by ablation of TNFR1 (11, 13). Cells derived from $Tbk1^{-/-}$ mice were reported to exhibit normal NF-κB activation without increased sensitivity to TNF-induced apoptosis (11). However, the present results show that TBK1 can directly phosphorylate RelA and thereby control the expression of a subset of NF-κB target genes that inhibit TNF-induced apoptosis. Our findings that $Tbk1^{-/-}$ MEFs are highly susceptible to TNF-induced apoptosis are consistent with the phenotype of $Tbk1^{-/-}$ fetuses, which exhibit all the characteristics of a defective TNF-induced and NF-κB–dependent antiapoptotic response (13). The divergence between our results and those reported earlier may result from different experimental conditions and detection methods. For instance, Bonnard et al. (11), examined cell viability by PI staining after stimulation of MEFs with a low dose of TNF (10 ng/mL), whereas we used a higher dose of TNF (25 ng/mL) without or with CHX and evaluated the apoptotic response by TUNEL assays and direct analysis of caspase-3 cleavage.

Molecular analysis of signaling events downstream of TNFR1 revealed that $Tbk1^{-/-}$ cells exhibit impaired IKK-mediated RelA phosphorylation at Ser^{534}, confirming the earlier suggestion that TBK1 modulates IKK activity (9). Importantly, expression of a phospho-mimic RelA(S534E) variant in $Tbk1^{-/-}$ MEFs restored the antiapoptotic response, demonstrating a specific biological function associated with RelA Ser^{534} phosphorylation, although this phosphorylation event is not critical for activation of most NF-κB target genes. These findings are consistent with previous reports that TNF-induced NF-κB activation is largely

normal in *Tbk1*$^{-/-}$ cells (11). Phosphorylation of RelA at Ser^{534} does not affect most RelA functions, including inhibition by IκBs, nuclear translocation, and binding to target gene promoters (Fig. S3). Instead, it modulates its ability to transactivate a specific subset of NF-κB target genes. Among these, we have identified *Pai-2* as a critical antiapoptotic gene and showed that reexpression of PAI-2 in *Tbk1*$^{-/-}$ MEFs inhibited the TNF-induced apoptotic response. Although NF-κB activation through induced IκB degradation is a well established signaling mechanism, it has long been suspected that expression of individual NF-κB target genes is further modulated through specific posttranslational modifications of NF-κB subunits (35, 36). We now show that one such mechanism involves RelA Ser^{534} phosphorylation, which depends on TBK1 and IKK activity. However, it is not yet clear how TBK1 directs IKK to specifically phosphorylate RelA Ser^{534} while having no effect on other IKK-dependent functions.

We also do not understand what causes the initial activation of caspase-8 in *Tbk1*$^{-/-}$ cells and how PAI-2 affects caspase-8 activation. We showed that cFLIP$_L$ is cleaved in a caspase-dependent manner when *Tbk1*$^{-/-}$ MEFs are stimulated with TNF in the presence of CHX (Fig. S1), and this may prompt initiation of the proapoptotic cascade. This is consistent with previous studies reporting that TNF promotes caspase-8 activation by elimination of cFLIP$_L$ when NF-κB–mediated *cFlip* induction is defective (5), de novo protein synthesis is blocked (37), or cFLIP degradation is enhanced (38). Furthermore, it was recently proposed that, in response to death receptor ligation, cFLIP and caspase-8 could form catalytically inactive heterodimers, which prevent the initiation of apoptosis (39).

Our results suggest that PAI-2 exerts its antiapoptotic function through interaction with and stabilization of TG2, which prevents caspase-3 activation by cross-linking of procaspase-3. Although it remains to be determined whether TG2 can also cross-link other caspases, including caspase-8, this observation provides a missing molecular link that explains the observation made more than a decade ago that the C-D interhelical domain or C-D loop of PAI-2, a conserved protein binding domain among ov-serpin family members (14), was essential for the antiapoptotic function of PAI-2 in TNF-stimulated cells (22). It was postulated that an interaction between the C-D loop and unknown proteins was likely to be important for resistance to apoptosis. We now show that PAI-2 interacts with TG2 in a TNF-dependent manner. This interaction presumably protects TG2 from proteolysis allowing TG2 to cross-link procaspase-3 and promote cell survival. Interestingly, another ubiquitously expressed ov-serpin family member, serpinB10 (PI10), was also found to provide protection against TNF-induced apoptosis (40). The authors observed the formation of high molecular weight SDS-stable PI10-containing complexes in cells treated with TNF in the presence of CHX (40). These complexes were suggested to contain a serine protease that is activated during this process, but this activity was never identified. Nevertheless, these observations raise the hypothesis that some ov-serpins may share a common function in controlling cell death, and that their specific physiological roles may have been obscured as a result of redundancy (14, 41). Although it remains to be further investigated, our observations that PAI-2 and TG2 interact in cells, and mediate a common antiapoptotic response, suggest that these unconventional antiapoptotic factors participate in a posttranslational mechanism that controls caspase-3 activation. Identification of the mechanism that controls TG2 turnover will provide additional insights into this antiapoptotic process.

The tumor suppressor retinoblastoma protein (Rb) is another intracellular target of PAI-2, which protects Rb from cleavage by calpains and thereby contributes to tumor cell survival (42). It was also shown that TG2 could protect Rb from caspase-7–mediated cleavage in fibroblasts (43). In light of our present results, it is tempting to speculate that PAI-2 and TG2 or a related enzyme may also control Rb-dependent cell survival. Notably, PAI-2 was also found to protect macrophages from pathogen-induced cell death (44), acting as a modulator of the innate immune response (45).

The antiapoptotic function of TG2 has been widely debated (25, 46), primarily because no spontaneous cell death was observed in *Tg2*$^{-/-}$ mice (31, 47, 48). However, TG2 protects cancer cells from thapsigargin- or hypoxia-induced death (23, 24), as well as staurosporine-induced apoptosis (49). Initial evidence for the antiapoptotic function of TG2 in vivo came from the work of Sarang et al. (26), who showed that *Tg2*$^{-/-}$ mice were more susceptible to Fas-mediated cell death. We now show in two different models of liver injury triggered by injection of TNF to Act D-sensitized mice or by Con A administration that *Tg2*$^{-/-}$ mice display increased hepatocyte apoptosis relative to WT counterparts (Fig. 5). These data strongly support a role for TG2 in inhibition of cell death mediated by members of the TNF/TNFR1 superfamily. However, an important question that needs to be answered is why *Pai-2*$^{-/-}$ and *Tg2*$^{-/-}$ mice are viable whereas genetic ablation of *Tbk1* leads to embryonic lethality. It could be argued that the newly identified PAI-2 and TG2-dependent pathway is not the only way by which TBK1 inhibits cell death. In addition, PAI-2 may act redundantly with PI10, as mentioned earlier. Furthermore, *Pai-2* is only one of several NF-κB–regulated antiapoptotic genes, such as *cIaps*, *cFlip*, *Bcl-X$_L$*, and others (5, 20), whose expression is needed to suppress TNF-induced liver destruction. Although the antiapoptotic function of these genes has never been disputed, genetic ablation of each one of them in isolation does not result in embryonic lethality as a result of liver failure. The current challenge is to identify the minimal set of antiapoptotic genes that needs to be expressed at a given time and in a particular environmental context during liver development and adult life to suppress TNF-driven hepatocyte death. It will also be interesting to test whether the combined ablation of both *Pai-2* and *Tg2* will result in a more severe phenotype that approaches that of *Tbk1*$^{-/-}$ mice. The identification of additional antiapoptotic factors whose expression or activity depends on TBK1 will shed further light on this question. Such factors may act independently of or in conjunction with the PAI-2–TG2 pathway.

Materials and Methods

Reagents. CHX, puromycin, z-VAD-FMK, MG-132, and protease inhibitors were from Calbiochem, and Act D, Con A, AEBSF, and Polybrene were from Sigma-Aldrich. Recombinant human PAI-2 was from Peprotech. Antibodies against RelA/p65 (S536) (no. 3031), phospho-IκBα (no. 9241), phospho-MAPKs (no. 9910), phospho-cJun (no. 9261), ERK, p38 (no. 9212), TBK1 (no. 3012), Bcl-X$_L$ (no. 2764), c-IAP1 (no. 4952), mBID (no. 2003), caspase-3 (no. 9662), cleaved caspase-3 (no. 9661), and cleaved PARP (no. 9544) were from Cell Signaling; antibodies to IKKγ (no. 557383), JNK1 (no. 551196), XIAP (no. 610716), CD95/Fas receptor (554254), caspase-8 (no. 559932), and procaspase-3 (no. 65906E) were from BD Transduction Laboratories; antibodies to IKKα (no. IMG-136A), IKKβ (no. IMG-129A), TBK1 (IMG-139A), and IκBα (no. IMG-127A) were from Imgenex; antibodies against RelA (sc-372 and sc-372-G), RelB, cRel, IκBβ, HSP60, and PAI-2 (sc-25746) were from Santa Cruz Biotechnology; anti-p65/RelA (CT), anti–phospho-ATF-2 (no. 05–891), anti-TG2 (no. 06–471), and anti-caspase-1 (no. 06–503) were from Upstate Biotechnology; anti–CREB-1 (AB3006) was from Millipore; anti-FLIPα (CT; no. 1161) was from ProSci, anti-TG2 (AB-4) was from Neomarkers (Lab Vision), anti-HA (clone 3F10) was from Roche, anti-cAIP2 was from R&D Systems, and anti-CD31 was from Abcam.

Immunoblotting. Whole-cell extracts were obtained by lysing cells in a buffer containing 50 mM Tris-HCl, pH 7.6, 250 mM NaCl, 1% Triton X-100, 0.5% Nonidet P-40, 3 mM EDTA, 3 mM EGTA, 10% glycerol, 2 mM DTT, 1 mM PMSF, 1 mM sodium orthovanadate, and a protease inhibitor mixture (Calbiochem). Nuclear extracts were prepared using NE-PER Nuclear and Cytoplasmic Extraction Reagents (Pierce). Proteins were separated by SDS/PAGE and blotted onto PVDF membranes (Millipore). The membranes were probed with the

appropriate antibodies and the antigen–antibody complexes detected by SuperSignal Western Pico Luminol/Enhancer solution (Pierce).

Kinase Assays. The IKK complex was immunoprecipitated from cell extracts using an anti-IKKγ antibody and the IKK activity was measured by in vitro kinase assay as described (19, 50) by using GST-IκBα(1-54) or GST-p65(354-551) as substrates.

Phosphorus-32 Metabolic Labeling and Phospho-Peptide Mapping. Cells were labeled with [^{32}P]orthophosphate as previously described (19, 50). Briefly, cells incubated with [^{32}P]orthophosphate (2 mCi/mL) for 5 h were stimulated with TNF (25 ng/mL) for 15 min, washed with PBS solution, and harvested in RIPA buffer. RelA was immunoprecipitated from precleared lysates by using an anti-RelA/p65 antibody (C-20; Santa Cruz Biotechnology). Immune complexes were washed in RIPA buffer. The proteins were resolved by SDS/PAGE and transferred to PVDF membranes (Millipore) for autoradiography and immunoblot analysis. Phospho-peptide mapping of phospho-labeled RelA/p65 was performed as described (19, 50).

Site-Directed Mutagenesis. Site-directed mutagenesis was performed using the Quick Exchange Mutagenesis kit (Stratagene) according to the manufacturer's instructions.

Retroviral Transductions. cDNAs were subcloned into the pLPCX retroviral vector (Stratagene). Recombinant retroviruses were produced by cotransfection with pCL-Eco into Phoenix packaging cells using Lipofectamine Plus reagent (Invitrogen). Supernatants containing recombinant retroviruses were collected 2 d after transfection, filtered to remove cell debris, and used directly for infection. MEFs at subconfluence were infected with viral stocks in the presence of Polybrene at 8 μg/mL, and two or three consecutive infections were performed over a period of 24 h. One day after the last infection, the infected cells were selected in medium supplemented with 2 μg/mL puromycin. Experiments were performed with pools of stable cells.

Gene Silencing Using shRNAs. Retroviral vectors (pRS plasmids) encoding shRNAs specific to mPAI-2 or a scrambled shRNA were purchased from Origene. Production of retroviruses, infection of cells and selection of stable cells were performed as described earlier. The most efficient *Pai-2*–specific shRNA construct among four tested was used.

Apoptosis Assays. Cells gown on Permanox Lab-Tek chamber slides were left untreated or stimulated with TNF (25 ng/mL) in the presence or absence of CHX (10 μg/mL) for the indicated times. Cells were fixed with 4% paraformaldehyde and permeabilized for 5 min with 0.1% Triton X-100 in 0.1% sodium citrate at 4 °C. Apoptotic cells were detected by TUNEL staining (Roche or Promega). DAPI staining was performed for total cell counting.

Immunofluorescence. Cells cultured on Lab-Tek chamber slides were left untreated or stimulated for 30 min with TNF (25 ng/mL). Cells were fixed with 4% paraformaldehyde, and the subcellular localization of RelA/p65 was examined by fluorescent immunostaining by using a polyclonal antibody against p65 (C-20) and Alexa-labeled anti-rabbit purified IgG (Jackson ImmunoResearch).

qRT-PCR and Microarray Analysis. Total RNA was extracted using TRIzol LS (Invitrogen) and purified on RNeasy Miniprep columns (Qiagen). For qRT-PCR analysis, cDNAs were synthesized by using a SuperScript II cDNA synthesis kit (Invitrogen). Real-time PCR amplifications were performed in 96-well optical reaction plates with Power SYBR Green PCR Master Mix (Applied Biosystems). Primers were designed by using Primer Express software. Primer sequences are available upon request. For microarray analysis, preparation of cDNA probes, hybridization to a mouse 10k oligo DNA microarray, scanning of the microarrays, and data analysis were performed by the Nippon Laser and Electronics Lab (Nagoya, Japan).

ChIP Assays. ChIP assays were performed as described (51) by using a polyclonal antibody against RelA/p65 (C-20; Santa Cruz Biotechnology). Samples were analyzed by PCR. Sequence information of the promoter-specific primers is available upon request.

In Vivo Transamidation. Assays were performed essentially as described previously (27). Cells were metabolically labeled with 1 mM pentylamine-biotin (BP; Pierce) added to the culture medium for 1 h before stimulation with TNF (25 ng/mL) for the indicated times. Cells were washed with PBS solution and harvested, and cell extracts were prepared by sonication in urea-containing buffer (50 mM Tris HCl, pH 7.6, 250 mM NaCl, 2 M urea, 0.05% SDS, 40 mM DTT, and a protease inhibitor mixture). Proteins were resolved by SDS/PAGE (10% gel) and transferred onto nitrocellulose membranes (Schleicher and Schuell), and proteins that incorporated BP were detected by using HRP-conjugated streptavidin and chemiluminescence (Pierce).

In Vitro Transamidation Assays. The mouse procaspase-3 cDNA was HA-tagged and subcloned into pBluescript KS(+) (Stratagene). The protein was expressed by in vitro coupled transcription-translation in reticulocyte lysate (Promega), immunoprecipitated with anti-HA beads (Roche), and eluted with HA-peptide. The protein was further incubated with PAI-2 or TG2 immunoprecipitated from cell extracts or with recombinant proteins in a buffer containing 50 mM Tris HCl, pH 8.5, 150 mM NaCl, 5 mM $CaCl_2$, and a protease inhibitor mixture (Calbiochem). The reactions were carried out for 1 h at 37 °C. HA-tagged procaspase-3 was detected by SDS/PAGE and immunoblotting using anti-HA or anti–procaspase-3 antibodies.

Mice. *Tg2*$^{-/-}$ mice were generated by homologous recombination (31) and were back-crossed to C57BL/6 mice for more than eight generations.

Preparation of MEFs. MEFs were prepared from individual littermate embryos at embryonic day 13.5 by using a standard procedure. Briefly, after removal of the head and the liver, the embryonic tissue was washed twice with PBS solution and treated with trypsin/EDTA for 30 min. The homogenates were transferred into a 150-mm dish containing complete culture medium (DMEM supplemented with 10% FBS, 0.1 mM β-mercaptoethanol, and antibiotics). Cells were passaged every 2 to 3 d. Experiments were performed with cells at passages three and four. The genotype of MEFS was determined and confirmed by PCR using genomic DNA extracted from yolk sac and MEFs.

Liver Injury Models. All experimental protocols were conducted in accordance with the Korean law on animal protection and approved by the institutional animal care and use committee at the National Cancer Center of Korea. Mice (9–10 wk old) were injected intraperitoneally with 20 μg of Act D and 0.3 μg of mouse TNF (no.575202; Biolegend). Alternatively, Con A was injected through the tail vein at 35 mg/kg. In both cases, PBS solution was injected in control animals. Mice were killed 8 h, 24 h (Con A), or 16 h (TNF and Act D) after challenge. Blood was collected by cardiac puncture, and the livers were surgically removed. Serum ALT and AST levels were determined by using Fuji Dri-Chem Slides AST-/ALT-PIII (FujiFilm) according to the manufacturer's instructions. Liver tissue samples were fixed in 10% buffered formalin and processed for paraffin embedding and histological evaluation. Pieces of liver tissue were snap-frozen and used for preparation of whole-liver protein extracts. Histological analysis was performed on liver sections (2–3 μm thick) after routine H&E staining. In situ TUNEL assays were performed on tissue sections by using an in situ apoptosis detection kit (Takara Bio) according to the manufacturer's instructions. Briefly, deparaffinized sections were treated with proteinase K and washed with PBS solution, and endogenous peroxidase activity was inactivated in 3% H_2O_2. After terminal-deoxynucleotidyl transferase enzymatic reaction, the signal was detected by using an HRP-labeled anti-FITC antibody and visualized with DAB as substrate.

Immunohistochemistry. Deparaffinized tissue sections were incubated with anti-CD31 (PECAM-1; Abcam) at a dilution of 1:50. Antibody binding was detected by using a HRP-linked secondary antibody and revealed by conventional immunostaining performed in an autoimmunostaining apparatus (HX System; Ventana) using DAB as substrate.

ACKNOWLEDGMENTS. We thank D. Rothwarf for critical reading of the manuscript and helpful suggestions; W.-C. Yeh, S. Akira, A. Beg, A. Hoffmann, R. Flavell, and Z.-W. Li for providing *Tbk1*$^{-/-}$, *RelA/p65*$^{-/-}$, *IκBα*$^{-/-}$, *caspase-3*$^{-/-}$, and *Ikkα/β*$^{-/-}$ MEFs, respectively; P. Brouckaert for providing mTNF; M. Hernandez (Applied Biosystems) for advice on quantitative PCR; C. H. Jeon for technical assistance; and D. Ginsburg, M. Montminy, T. Kato, and S. Imajoh-Ohmi for plasmids and antibodies. M.D. was supported by a grant from the Claudia Adams Barr Program in Cancer Research. K.S.K. was supported by the National Institutes of Health (NIH). This work was supported by National Cancer Center (Korea) Research Grants NCC 0510270 and NCC1110011-1 (to H.L. and S-Y.K.), National Research Foundation Grant 2010-0029919 funded by the Korean government (to S-Y.K.), NIH Grant AI043477 (to M.K.), and Grants-in-Aid for Scientific Research on Priority Area and for Scientific Research (B) by the Ministry of Education, Science, Sports, and Culture of Japan (M.N.), M.K. is an American Cancer Society Research Professor.

1. Green DR, Evan GI (2002) A matter of life and death. *Cancer Cell* 1:19–30.
2. Li J, Yuan J (2008) Caspases in apoptosis and beyond. *Oncogene* 27:6194–6206.
3. Chen G, Goeddel DV (2002) TNF-R1 signaling: A beautiful pathway. *Science* 296: 1634–1635.
4. Wajant H, Scheurich P (2011) TNFR1-induced activation of the classical NF-κB pathway. *FEBS J* 278:862–876.
5. Karin M, Lin A (2002) NF-kappaB at the crossroads of life and death. *Nat Immunol* 3: 221–227.
6. Burstein E, Duckett CS (2003) Dying for NF-kappaB? Control of cell death by transcriptional regulation of the apoptotic machinery. *Curr Opin Cell Biol* 15:732–737.
7. Janes KA, et al. (2006) The response of human epithelial cells to TNF involves an inducible autocrine cascade. *Cell* 124:1225–1239.
8. Pomerantz JL, Baltimore D (1999) NF-kappaB activation by a signaling complex containing TRAF2, TANK and TBK1, a novel IKK-related kinase. *EMBO J* 18:6694–6704.
9. Tojima Y, et al. (2000) NAK is an IkappaB kinase-activating kinase. *Nature* 404: 778–782.
10. Kuai J, et al. (2004) NAK is recruited to the TNFR1 complex in a TNFalpha-dependent manner and mediates the production of RANTES: identification of endogenous TNFR-interacting proteins by a proteomic approach. *J Biol Chem* 279:53266–53271.
11. Bonnard M, et al. (2000) Deficiency of T2K leads to apoptotic liver degeneration and impaired NF-kappaB-dependent gene transcription. *EMBO J* 19:4976–4985.
12. Hemmi H, et al. (2004) The roles of two IkappaB kinase-related kinases in lipopolysaccharide and double stranded RNA signaling and viral infection. *J Exp Med* 199:1641–1650.
13. Gerondakis S, et al. (2006) Unravelling the complexities of the NF-kappaB signalling pathway using mouse knockout and transgenic models. *Oncogene* 25:6781–6799.
14. Izuhara K, Ohta S, Kanaji S, Shiraishi H, Arima K (2008) Recent progress in understanding the diversity of the human ov-serpin/clade B serpin family. *Cell Mol Life Sci* 65:2541–2553.
15. Liu ZG, Hsu H, Goeddel DV, Karin M (1996) Dissection of TNF receptor 1 effector functions: JNK activation is not linked to apoptosis while NF-kappaB activation prevents cell death. *Cell* 87:565–576.
16. Tang G, et al. (2001) Inhibition of JNK activation through NF-kappaB target genes. *Nature* 414:313–317.
17. Fujita F, et al. (2003) Identification of NAP1, a regulatory subunit of IkappaB kinase-related kinases that potentiates NF-kappaB signaling. *Mol Cell Biol* 23:7780–7793.
18. Buss H, et al. (2004) Constitutive and interleukin-1-inducible phosphorylation of p65 NF-kappaB at serine 536 is mediated by multiple protein kinases including IkappaB kinase (IKK)-alpha, IKKbeta, IKKepsilon, TRAF family member-associated (TANK)-binding kinase 1 (TBK1), and an unknown kinase and couples p65 to TATA-binding protein-associated factor II31-mediated interleukin-8 transcription. *J Biol Chem* 279: 55633–55643.
19. Delhase M, Hayakawa M, Chen Y, Karin M (1999) Positive and negative regulation of IkappaB kinase activity through IKKbeta subunit phosphorylation. *Science* 284: 309–313.
20. Pahl HL (1999) Activators and target genes of Rel/NF-kappaB transcription factors. *Oncogene* 18:6853–6866.
21. Kumar S, Baglioni C (1991) Protection from tumor necrosis factor-mediated cytolysis by overexpression of plasminogen activator inhibitor type-2. *J Biol Chem* 266: 20960–20964.
22. Dickinson JL, Norris BJ, Jensen PH, Antalis TM (1998) The C-D interhelical domain of the serpin plasminogen activator inhibitor-type 2 is required for protection from TNF-alpha induced apoptosis. *Cell Death Differ* 5:163–171.
23. Yamaguchi H, Wang HG (2006) Tissue transglutaminase serves as an inhibitor of apoptosis by cross-linking caspase 3 in thapsigargin-treated cells. *Mol Cell Biol* 26: 569–579.
24. Jang GY, et al. (2010) Transglutaminase 2 suppresses apoptosis by modulating caspase 3 and NF-kappaB activity in hypoxic tumor cells. *Oncogene* 29:356–367.
25. Lorand L, Graham RM (2003) Transglutaminases: Crosslinking enzymes with pleiotropic functions. *Nat Rev Mol Cell Biol* 4:140–156.
26. Sarang Z, et al. (2005) Tissue transglutaminase (TG2) acting as G protein protects hepatocytes against Fas-mediated cell death in mice. *Hepatology* 42:578–587.
27. Shin DM, et al. (2004) Cell type-specific activation of intracellular transglutaminase 2 by oxidative stress or ultraviolet irradiation: implications of transglutaminase 2 in age-related cataractogenesis. *J Biol Chem* 279:15032–15039.
28. Lakhani SA, et al. (2006) Caspases 3 and 7: Key mediators of mitochondrial events of apoptosis. *Science* 311:847–851.
29. Masud A, et al. (2007) Endoplasmic reticulum stress-induced death of mouse embryonic fibroblasts requires the intrinsic pathway of apoptosis. *J Biol Chem* 282: 14132–14139.
30. Siegel M, Khosla C (2007) Transglutaminase 2 inhibitors and their therapeutic role in disease states. *Pharmacol Ther* 115:232–245.
31. Kim DS, et al. (2010) Transglutaminase 2 gene ablation protects against renal ischemic injury by blocking constant NF-κB activation. *Biochem Biophys Res Commun* 403: 479–484.
32. Napolitano G, Karin M (2010) Sphingolipids: The oil on the TRAFire that promotes inflammation. *Sci Signal* 3:pe34.
33. Chariot A, et al. (2002) Association of the adaptor TANK with the I kappa B kinase (IKK) regulator NEMO connects IKK complexes with IKK epsilon and TBK1 kinases. *J Biol Chem* 277:37029–37036.
34. Bouwmeester T, et al. (2004) A physical and functional map of the human TNF-alpha/NF-kappa B signal transduction pathway. *Nat Cell Biol* 6:97–105.
35. Ghosh S, Karin M (2002) Missing pieces in the NF-kappaB puzzle. *Cell* 109(suppl): S81–S96.
36. Perkins ND (2006) Post-translational modifications regulating the activity and function of the nuclear factor kappa B pathway. *Oncogene* 25:6717–6730.
37. Wang L, Du F, Wang X (2008) TNF-alpha induces two distinct caspase-8 activation pathways. *Cell* 133:693–703.
38. Chang L, et al. (2006) The E3 ubiquitin ligase itch couples JNK activation to TNFalpha-induced cell death by inducing c-FLIP(L) turnover. *Cell* 124:601–613.
39. Green DR, Oberst A, Dillon CP, Weinlich R, Salvesen GS (2011) RIPK-dependent necrosis and its regulation by caspases: A mystery in five acts. *Mol Cell* 44:9–16.
40. Schleef RR, Chuang TL (2000) Protease inhibitor 10 inhibits tumor necrosis factor alpha -induced cell death. Evidence for the formation of intracellular high M(r) protease inhibitor 10-containing complexes. *J Biol Chem* 275:26385–26389.
41. Dougherty KM, et al. (1999) The plasminogen activator inhibitor-2 gene is not required for normal murine development or survival. *Proc Natl Acad Sci USA* 96: 686–691.
42. Tonnetti L, et al. (2008) SerpinB2 protection of retinoblastoma protein from calpain enhances tumor cell survival. *Cancer Res* 68:5648–5657.
43. Boehm JE, Singh U, Combs C, Antonyak MA, Cerione RA (2002) Tissue transglutaminase protects against apoptosis by modifying the tumor suppressor protein p110 Rb. *J Biol Chem* 277:20127–20130.
44. Park JM, et al. (2005) Signaling pathways and genes that inhibit pathogen-induced macrophage apoptosis—CREB and NF-kappaB as key regulators. *Immunity* 23: 319–329.
45. Medcalf RL (2011) Plasminogen activator inhibitor type 2: Still an enigmatic serpin but a model for gene regulation. *Methods Enzymol* 499:105–134.
46. Fesus L, Piacentini M (2002) Transglutaminase 2: An enigmatic enzyme with diverse functions. *Trends Biochem Sci* 27:534–539.
47. De Laurenzi V, Melino G (2001) Gene disruption of tissue transglutaminase. *Mol Cell Biol* 21:148–155.
48. Nanda N, et al. (2001) Targeted inactivation of Gh/tissue transglutaminase II. *J Biol Chem* 276:20673–20678.
49. Rossin F, D'Eletto M, Macdonald D, Farrace MG, Piacentini M (2011) TG2 transamidating activity acts as a reostat controlling the interplay between apoptosis and autophagy. *Amino Acids,* 10.1007/s00726-011-0899-x.
50. Delhase M (2003) IkappaB kinase and NF-kappaB signaling in response to pro-inflammatory cytokines. *Methods Mol Biol* 225:7–17.
51. Saccani S, Pantano S, Natoli G (2002) p38-Dependent marking of inflammatory genes for increased NF-kappa B recruitment. *Nat Immunol* 3:69–75.

Correction

CELL BIOLOGY

Correction for "TANK-binding kinase 1 (TBK1) controls cell survival through PAI-2/serpinB2 and transglutaminase 2," by Mireille Delhase, Soo-Youl Kim, Ho Lee, Aya Naiki-Ito, Yi Chen, Eu-Ree Ahn, Kazuhiro Murata, Se-Jin Kim, Norman Lautsch, Koichi S. Kobayashi, Tomoyuki Shirai, Michael Karin, and Makoto Nakanishi, which appeared in issue 4, January 24, 2012, of *Proc Natl Acad Sci USA* (109:E177–E186; first published December 27, 2011; 10.1073/pnas.1119296109).

The authors note that Figs. 1*C* (*Bottom*), 2*A*, 2*C*, 3*F*, and 4*E* have been revised to include dividing lines between lanes to show where extraneous data have been removed. These changes do not affect the data presented nor the conclusions of the article. The changes were made to comply with the PNAS policy that requires dividing lines whenever entire nonessential lanes have been removed from a single original gel. The corrected figures appear below.

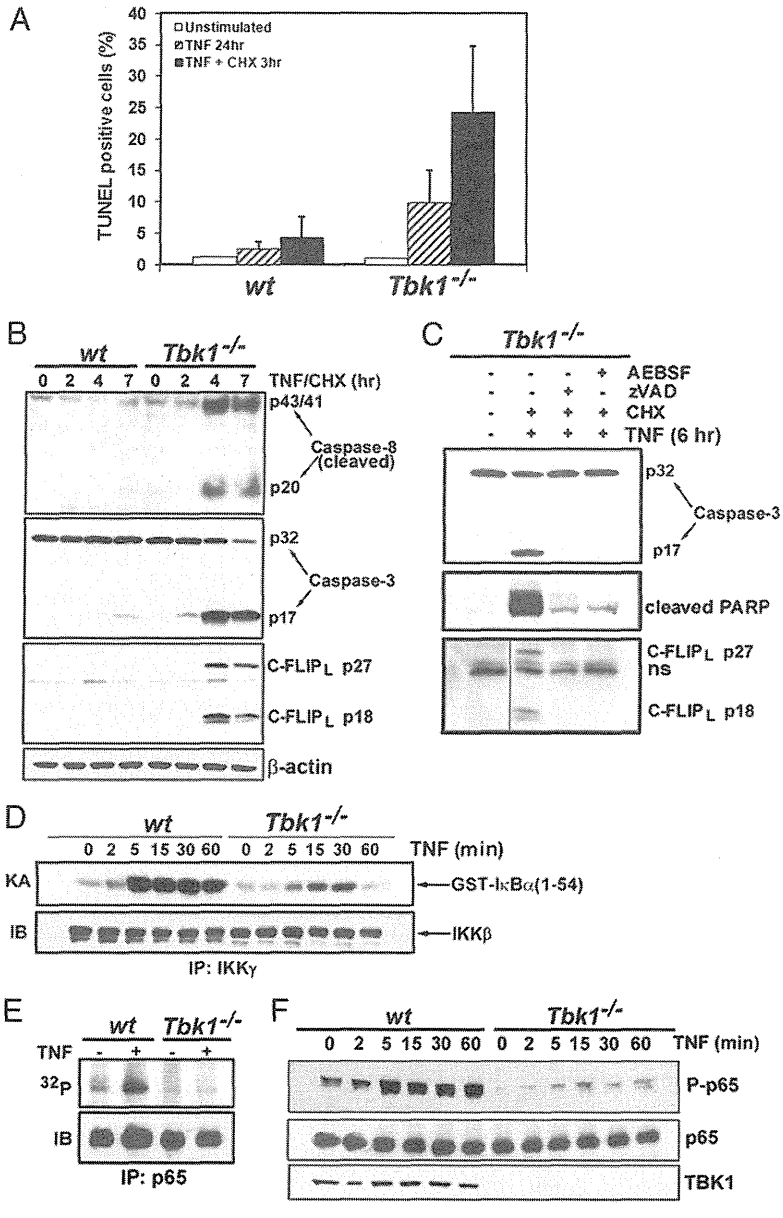

Fig. 1.

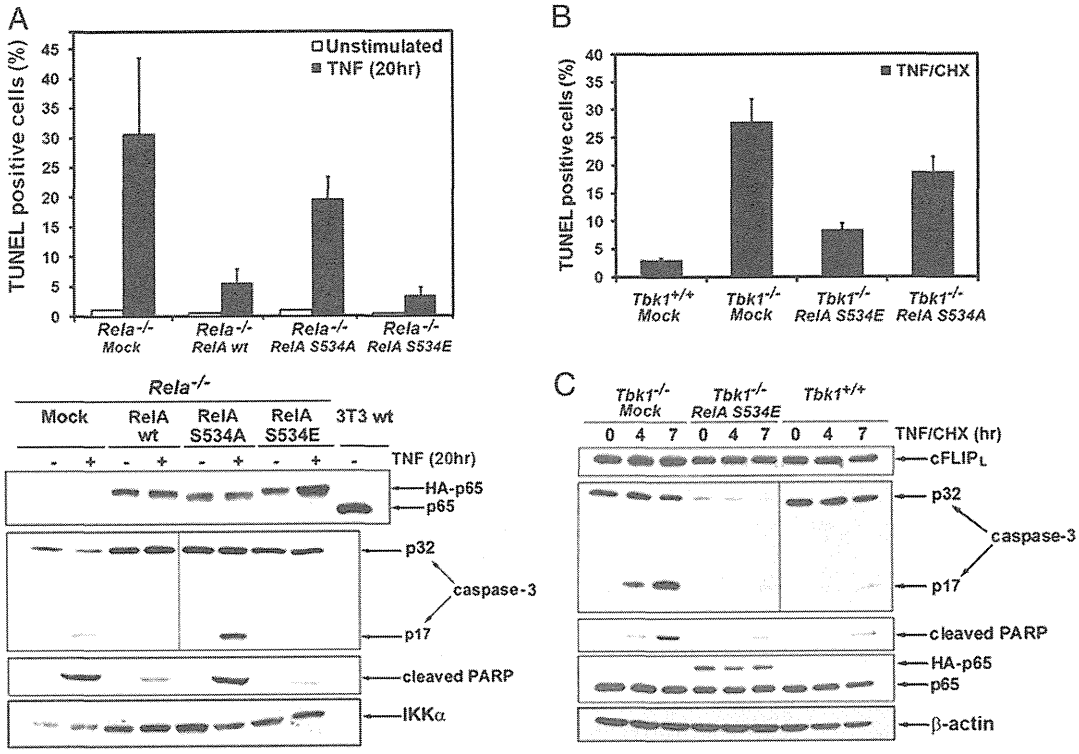

Fig. 2.

CORRECTION

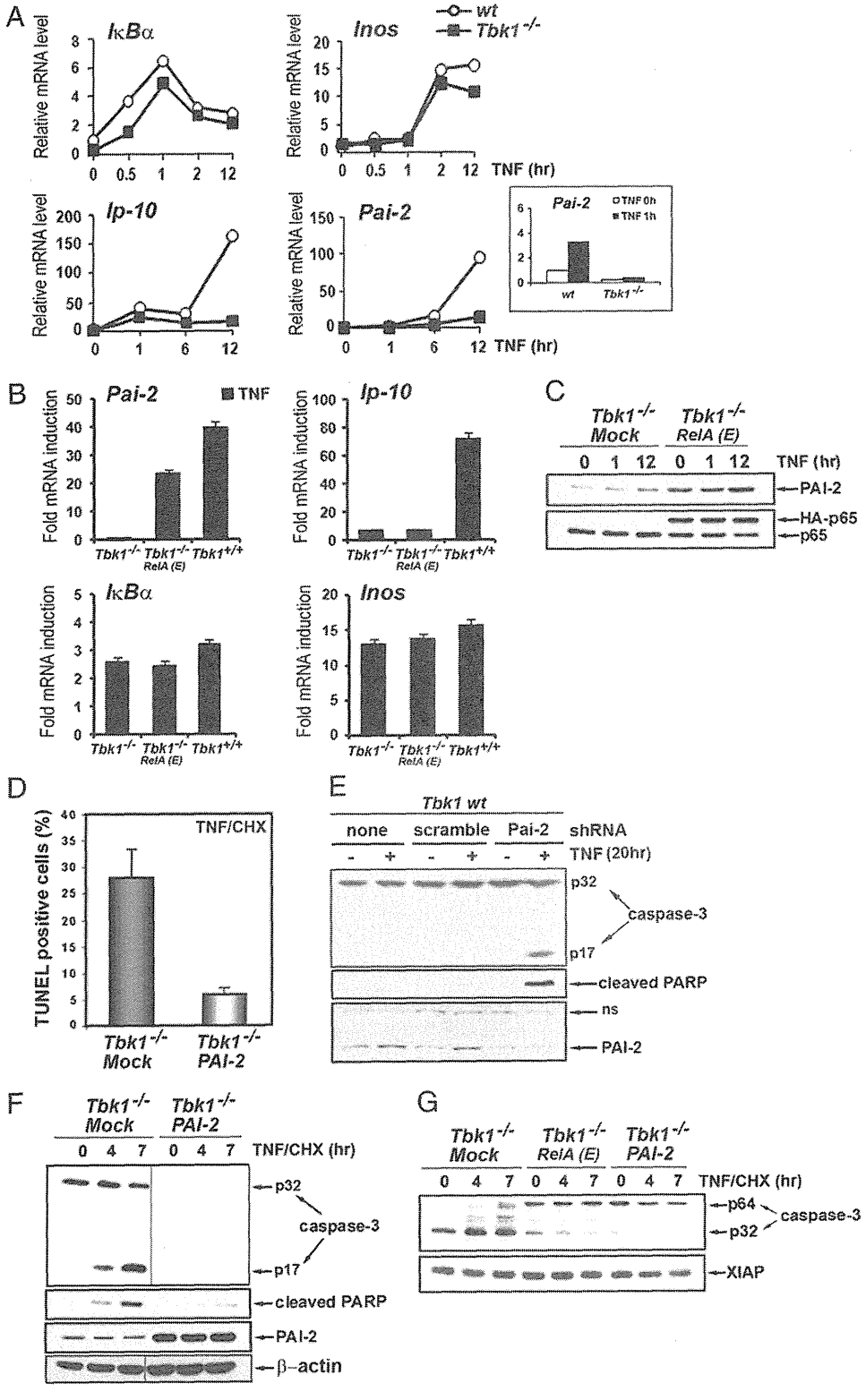
A
IκBα
Inos
wt
Tbk1 -/-
Ip-10
Pai-2
Relative mRNA level
TNF (hr)
TNF 0h
TNF 1h
B
Pai-2
TNF
Ip-10
IκBα
Inos
Fold mRNA induction
Tbk1 -/-
Tbk1 -/- RelA (E)
Tbk1 +/+
C
Tbk1 -/- Mock
Tbk1 -/- RelA (E)
TNF (hr)
PAI-2
HA-p65
p65
D
TUNEL positive cells (%)
TNF/CHX
Tbk1 -/- Mock
Tbk1 -/- PAI-2
E
Tbk1 wt
none
scramble
Pai-2
shRNA
TNF (20hr)
p32
caspase-3
p17
cleaved PARP
ns
PAI-2
F
Tbk1 -/- Mock
Tbk1 -/- PAI-2
TNF/CHX (hr)
p32
caspase-3
p17
cleaved PARP
PAI-2
β-actin
G
Tbk1 -/- Mock
Tbk1 -/- RelA (E)
Tbk1 -/- PAI-2
TNF/CHX (hr)
p64
p32
caspase-3
XIAP

Fig. 3.

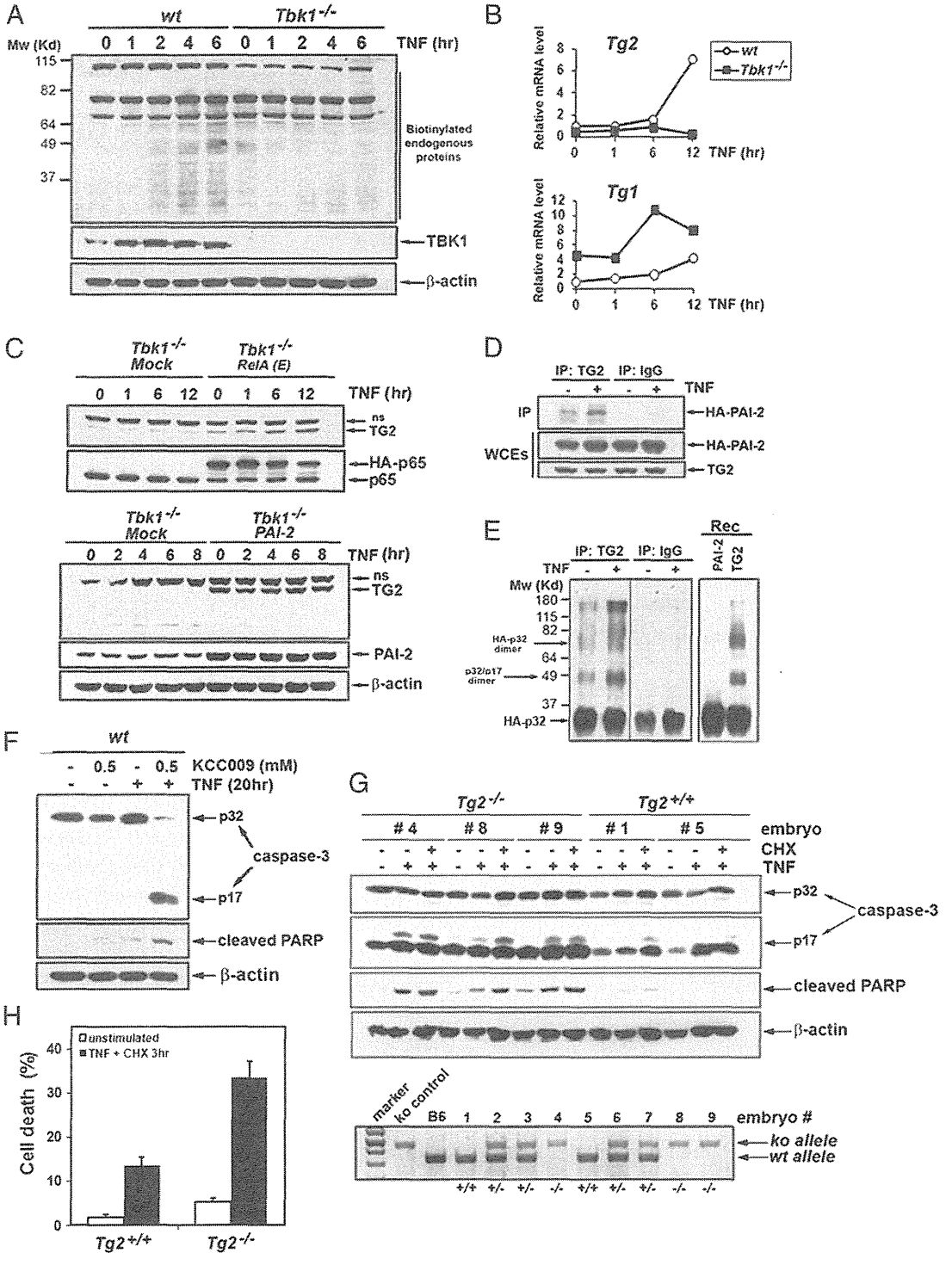

Fig. 4.

www.pnas.org/cgi/doi/10.1073/pnas.1201576109

Surg Today (2012) 42:46–51
DOI 10.1007/s00595-011-0021-8

ORIGINAL ARTICLE

Total resection of the right hepatic vein drainage area with the aid of three-dimensional computed tomography

Akinobu Taketomi · Kazuki Takeishi · Yohei Mano · Takeo Toshima · Takashi Motomura · Shinichi Aishima · Hideaki Uchiyama · Tomoharu Yoshizumi · Ken Shirabe · Yoshihiko Maehara

Received: 1 September 2010 / Accepted: 11 January 2011 / Published online: 11 November 2011

Abstract
Purpose We analyzed the feasibility and safety of our preliminary surgical approach for total hepatic resection of the right hepatic vein drainage area (THR-RHV) with the aid of three-dimensional computed tomography (3D-CT) guidance.
Methods Clinical findings and 3D-CT volumetry results were investigated in five patients who underwent THR-RHV for a hepatic malignant tumor close to the right hepatic vein (RHV).
Results The mean estimated remnant liver volume after a conventional right lobectomy was 474 ml, whereas that after THR-RHV was 614 ml, indicating that 140 ml (13.8%) of additional liver volume had been preserved by performing THR-RHV. The median operative time, mean ischemic time, and mean blood loss during surgery were 406 min, 51 min, and 587 ml, respectively. Histological examinations confirmed a negative surgical margin in all five patients. The mean liver volume estimated by 3D-CT was 458 ml, whereas the mean actual resected liver volume was 468 g, resulting in a mean error ratio of 3.1%.
Conclusions THR-RHV allowed for a higher remnant liver volume than that after conventional right lobectomy of the liver, and proved feasible with acceptable perioperative results. This technique thus promotes both safety and curability for patients with a tumor close to the RHV.

Keywords Computer-assisted three-dimensional imaging · Hepatectomy · Hepatic vein

A. Taketomi (✉) · K. Takeishi · T. Toshima · T. Motomura · H. Uchiyama · T. Yoshizumi · K. Shirabe · Y. Maehara
Department of Surgery and Science,
Graduate School of Medical Sciences,
Kyushu University, 3-1-1 Maidashi, Higashi-ku,
Fukuoka 812-8582, Japan
e-mail: taketomi@surg2.med.kyushu-u.ac.jp

Y. Mano · S. Aishima
Department of Surgical Pathology,
Graduate School of Medical Sciences,
Kyushu University, 3-1-1 Maidashi, Higashi-ku,
Fukuoka 812-8582, Japan

Introduction

Postoperative liver failure is a life-threatening complication of hepatic resection. Despite improvements in surgical instruments, techniques, and perioperative management, postoperative liver failure is still a major cause of mortality after hepatic resection [1, 2]. Our previous study using a volumetric analysis revealed the remnant liver volume (RmLV) of patients who died of liver failure to be significantly smaller than that of the patients who survived [3]. Consequently, it is important to preserve sufficient RmLV after hepatic resection.

The optimal surgical method to resect a tumor located close to the right hepatic vein (RHV) remains unclear, as limited resection for patients with impaired liver function may result in a positive surgical margin, whereas extended hepatic resection can result in hepatic insufficiency. When liver surgeons encounter such tumors, they face a dilemma between patient safety and curability. To overcome this a number of techniques, including preoperative portal embolization and hepatic vein reconstruction, have been reported [4–6]. However, these techniques cannot be applied to all patients.

Cho et al. [7] recently proposed a reclassification of the liver anatomy, in which the right anterior segment is divided into the ventral and dorsal segments by the anterior fissure. According to this new classification, the posterior

segment and the dorsal segment are drained by the RHV, then the ventral segment is drained by the middle hepatic vein (MHV) [8]. Based on this concept, they proposed various types of hepatic resection, including total resection of the RHV (THR-RHV) [7, 9]. In 2004, Kondo et al. [10] also described a novel surgical approach, called venous-drainage-guided selective hepatectomy. Based on the hepatic vein drainage area, we have been performing THR-RHV for the treatment of tumors close to the RHV. We present the results of our preliminary surgical approach in five patients who underwent THR-RHV with the aid of three-dimensional computed tomography (3D-CT) guidance, analyzing its feasibility, safety, and effectiveness.

Patients and methods

Patients

The subjects were five patients who underwent surgery for a hepatic malignant tumor close to the RHV trunk (Fig. 1) at Kyushu University Hospital, Fukuoka, Japan, between November 2008 and May 2009.

Preoperative simulation by 3D-CT

The methods used to conduct the preoperative evaluation of the liver volume and liver anatomy have been described previously [11, 12]. In brief, preoperative multidetector helical computed tomography (CT) images were made using 2-mm-thick slices represented on a CT machine. For enhancement, an intravenous bolus of contrast nonionic medium (Iopamrion; Schering, Erlangen, Germany) was given at a speed of 5 ml/s. This method allows for the clear visualization of the hepatic arteries, portal veins, and hepatic veins including RHV tributaries. Three-dimensional reconstructions of the liver were created with multidetector helical CT using the 3D-CT software, Zio M900 (Zio Software, Tokyo, Japan), which calculated the total liver volume (TLV) and the volume of the territories of both the portal and hepatic vein branches, from their diameter and length. We previously reported the accuracy of this software with a 9.6% mean error ratio [12]. The TLV, the resected liver volume (RsLV), and the RmLV were estimated in each case. The volumetric parameters were calculated for the two types of hepatic resection; namely, right lobectomy and THR-RHV (Fig. 2).

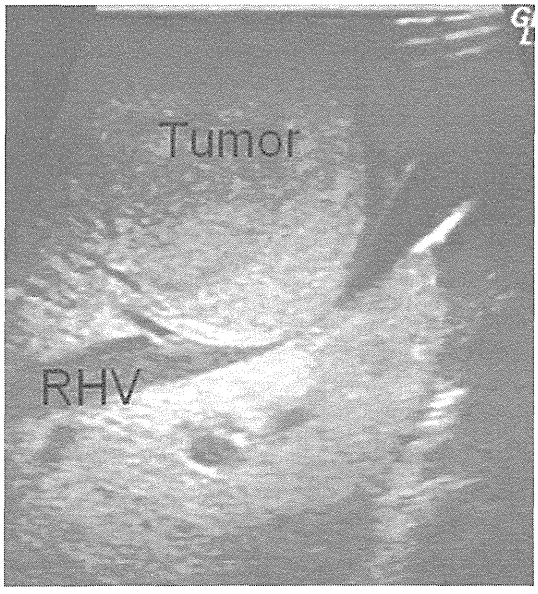

Fig. 1 Ultrasonography of the patients who underwent total hepatic resection of the right hepatic vein drainage area (THR-RHV). The right hepatic vein (*RHV*) was compressed by hepatocellular carcinoma

Operative technique for THR-RHV

This operation was performed via a midline and right subcostal laparotomy, with routine intraoperative ultrasonography to detect any differences from the preoperative imaging findings in relation to the tumor location and the vessel abnormalities. After removing the gallbladder in the usual manner, we used vessel tape to encircle the root of the right Glissonean pedicle, the anterior and posterior Glissonean pedicles, the RHV (extraparenchymally), and the right hepatic artery. For conventional right hepatic lobectomy (Fig. 3a) or posterior segmentectomy (Fig. 3b), only the Glissonean pedicle was clamped, so we could recognize the objective area. The drainage area of the RHV could then be recognized by the discoloration of the liver surface when the hepatic artery and the RHV were clamped simultaneously (Fig. 3c) [13]. After the root of the posterior Glissonean pedicle was ligated and divided, we mobilized the right hemiliver by ligating and dividing each short hepatic vein. A parenchymal transection was thus performed under intermittent clamping by hemivascular exclusion, which proceeded from the veno-occlusive line. The anterior fissure was opened more widely toward the cranial side, and the dorsal branches originating from the anterior trunk were ligated and divided one by one (Fig. 3d). Each vessel thicker than 2 mm was ligated with thin sutures. Finally, the root of the RHV was divided and continuously sutured to prevent stenosis of the inferior vena cava. The cut surface of the liver was secured with 3/4-0 sutures and electrocautery. To ensure there was no bile leakage, we conducted a bile leakage test of the resection area, using a solution of indocyanine green [14]. A closed suction drain was inserted into the abdominal cavity. This drain was removed within the first 3 postoperative days (PODs) when the bilirubin level in the drainage fluid was equal to or lower than the serum level.

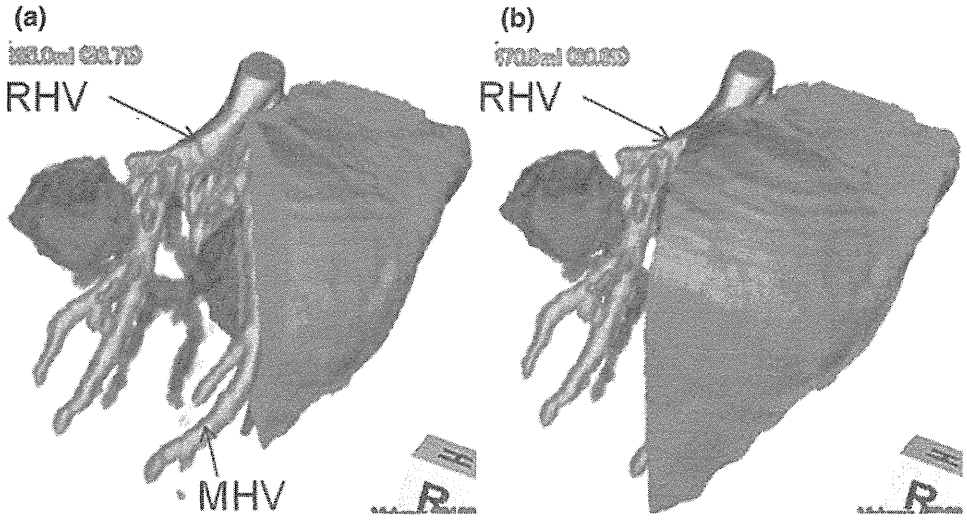

Fig. 2 Three-dimensional computed tomography (3D-CT) volumetric analysis. **a** Simulation for the right lobectomy. The estimated remnant liver volume was 285 g, representing 36.7% of the total liver volume (TLV). **b** Simulation for the THR-RHV. The estimated remnant liver volume was 471 g, representing 60.6% of the TLV. *RHV* right hepatic vein, *MHV* middle hepatic vein

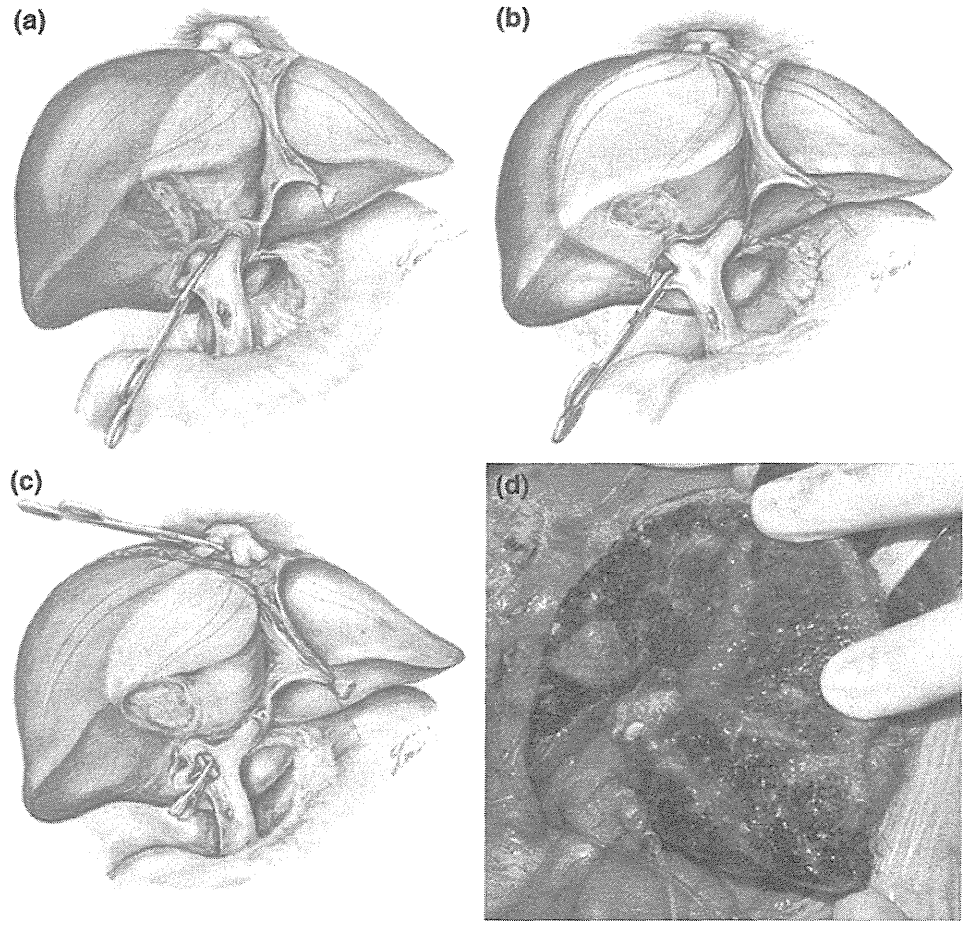

Fig. 3 Procedures for THR-RHV. **a** The demarcation line of the right lobe was recognized by clamping the right Glissonean sheath. **b** The demarcation line of the posterior segment was recognized by clamping the posterior Glissonean sheath. **c** The drainage area of the RHV was recognized by the discoloration of the liver surface when the hepatic artery and the RHV were simultaneously clamped. **d** Residual liver after THR-RHV. The right anterior branch of the Glissonean sheath was preserved on the cutting surface, while dividing the dorsal branch

Results

Preoperative 3D-CT volumetric analysis

The volumetric parameters calculated by 3D-CT, of the patients who underwent THR-RHV, are summarized in Table 1. Four of the five patients had hepatocellular carcinoma and one had a metastatic liver tumor from colon cancer. All of the tumors were located close to the RHV, and the mean size was 3.2 cm (range 1.8–4.7 cm). The mean estimated volume of the TLV was 1075 ml. As right lobectomy of the liver is the classic procedure for removing

Table 1 Clinical characteristics of the patients who underwent total hepatic resection of the right hepatic vein drainage area (THR-RHV)

Patient no.	Age (years)/sex	Disease	$ICGR_{15}$ (%)	Child–Pugh classification	Tumor size (cm)	TLV (ml)	Calculated RmLV after RL (ml)	Calculated RmLV after THR-RHV (ml)
1	64/male	HCC	14.3	A	3.5	1239	635 (51.2%)[a]	772 (62.3%)
2	60/male	HCC	5.8	A	2.6	1322	429 (32.5%)	603 (45.6%)
3	67/male	Meta	7.4	A	4.7	777	285 (36.7%)	471 (60.6%)
4	40/male	HCC	11.3	A	1.8	1324	655 (49.5%)	797 (60.2%)
5	87/female	HCC	10.4	A	3.6	714	365 (51.2%)	429 (61.1%)

HCC hepatocellular carcinoma, *ICG R-15* indocyanine green retention at 15 min, *Meta* metastatic liver cancer, *THR-RHV* total hepatic resection of right hepatic vein drainage area, *RL* right lobectomy, *RmLV* remnant liver volume, *TLV* total liver volume

[a] Percentage for the TLV

Table 2 Surgical outcomes and volumetric analysis of the patients who underwent total hepatic resection of the right hepatic vein drainage area (THR-RHV)

Patient no.	Operating time (min)	Ischemic time (min)	Blood loss (ml)	Transfusion (ml)	Max ALT (U/l)	Hospital stay (days)	SM (mm)	Calculated RsLV (ml)	RsLV (g)	Error ratio (%)[a]
1	300	48	315	0	96	9	Negative, 7	467	470	0.6
2	483	98	1040	0	556	10	Negative, 20	719	706	1.8
3	368	44	783	0	364	25	Negative, 6	306	305	0.3
4	488	33	203	0	393	8	Negative, 30	527	572	7.9
5	389	30	594	0	363	18	Negative, 2	273	287	4.9

ALT alanin aminotransferase, *SM* surgical margin, *RsLV* resected liver volume, *THR-RHV* total hepatic resection of the right hepatic vein drainage area

[a] Calculated as follows: error ratio (%) = |(RsLV − calculated RsLV)/RsLV| × 100

a tumor close to the RHV, we calculated the RmLV after right lobectomy versus that after THR-RHV, and found these values to be 474 ml (range 285–655 ml) versus 614 ml (range 429–797 ml), respectively. This indicated that 140 ml (13.8%) of additional RmLV had been preserved by performing THR-RHV for a tumor close to the RHV.

Postoperative outcomes after THR-RHV

The surgical outcomes of the patients who underwent THR-RHV are summarized in Table 2. The median operative time was 406 min (range 300–488 min), the mean ischemic time for the liver during the parenchymal transection was 51 min (range 30–98 min), and the mean blood loss during surgery was 587 ml (range 203–1040 ml). No patients required blood transfusion during or after surgery. One patient suffered drug-induced liver dysfunction (patient 3), but recovered with medical treatment. The mean hospital stay after surgery was 14 days (range 8–25 days). The mean distance of the surgical margins was 13 mm (range 2–30 mm), and histological examinations confirmed negative surgical margins in all patients (Fig. 4).

To assess the accuracy of the preoperative 3D-CT simulation for THR-RHV, the RsLV was compared with the estimated volume in each patient (Table 2). The mean estimated liver volume after THR-RHV was 458 ml (range 273–719 ml), whereas the mean actual RsLV was 468 g (range 287–706 g). The mean error ratio was 3.1% (range 0.3%–7.9%).

Discussion

The results of this study clearly showed the feasibility of performing THR-RHV with the aid of 3D-CT guidance. By using this technique, we were able to conserve the RmLV by 140 ml (13.8%) more than with conventional right lobectomy. Moreover, histological examination confirmed a negative surgical margin in all five patients who underwent THR-RHV, and the mean error ratio was only 3.1% between the estimated volume by 3D-CT and the actual RsLV.

Virtual hepatic resection using 3D-CT image analysis software based on the hepatic circulation has been developed only recently [15]. In fact, 3D-CT volumetric studies are now used widely in the field of living donor liver transplantation, because precise information about the liver volume and anatomical variations of the hepatic vessels must be obtained for the preoperative planning of safe

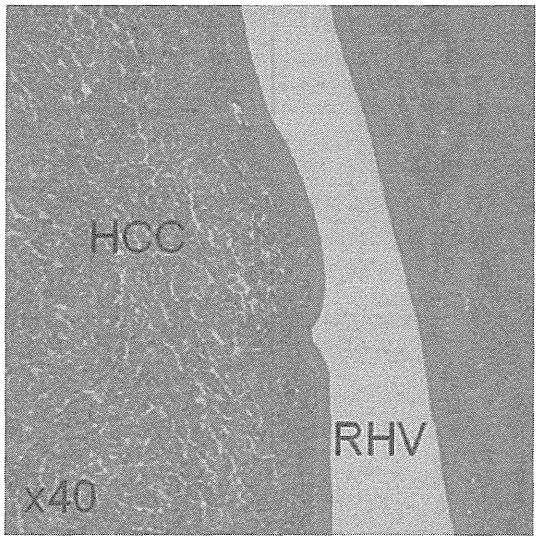

Fig. 4 Histological examination of the resected specimen. Moderately differentiated hepatocellular carcinoma growing in a trabecular pattern was recognized close to the hepatic vein. *HCC* hepatocellular carcinoma, *RHV* right hepatic vein (H&E ×40)

donor hepatectomy and successful transplantation [16, 17]. Saito et al. [15] presented precise data to show that the predicted liver resection volume was significantly correlated with the actual value, with a mean difference of 9.3 ml. We previously reported the mean error ratio for the age-adjusted formula for the procured liver graft to be only 9.6% [12]. The current study showed that the mean estimated liver volume after THR-RHV was comparable to the mean RsLV, indicating that the mean error ratio was only 3.1%. These findings suggest that the current 3D-CT volumetric study reliably estimated the RsLV, and confirmed preoperatively the benefits of performing venous-drainage-guided hepatectomy, such as THR-RHV.

As THR-RHV is a new surgical approach based on the venous drainage area, its safety and surgical outcomes still need to be verified. In the current series the surgical parameters, including the operative time, ischemic time, operative blood loss, and hospital stay after surgery, were comparable with those for similar patients undergoing right lobectomy (data not shown). Furthermore, histological examinations confirmed a negative surgical margin of malignant cells in all patients. Tanaka et al. [18] reported excellent short- and long-term results in 11 patients who underwent right hemihepatectomy with preservation of the ventral right anterior section guided by hepatic venous drainage. Kaneko et al. [19] found that the congested volume of the MHV drainage area was associated with high alanine aminotransferase levels after left liver harvesting with the MHV. Kido et al. [20] also showed the importance of hepatic drainage in liver regeneration. The mean volume increase of the medial segment on POD 90 was only 7% in extended right-lobe donors versus 61% in right-lobe donors, demonstrating a lower value in remnant livers without MHV. These findings show the importance of hepatic vein drainage for liver regeneration after hepatic resection, thus making it possible to prevent hepatic insufficiency and/or hepatic failure. As THR-RHV leaves no congestive area in the remnant liver and it increases the volume of the remnant liver, we believe that it is a feasible and effective surgical approach for tumors close to the RHV.

THR-RHV requires no special surgical techniques or equipment. In the present study, when the hepatic artery and the RHV were exposed following their simultaneous clamping, we recognized the drainage area of the RHV by the discoloration of the liver surface (Fig. 3c) [13]. This was achieved easily in all five patients; however, this technique may not be applicable for a patient with an anatomical variation of the hepatic artery or hepatic vein. Thus, further studies on a large number of patients are needed to assess the applicability of this technique. One of the most important aspects of this surgical technique is the exposure of the right anterior Glissonean pedicle on the parenchymal dissection plane [10]. As shown in Fig. 3d, the dorsal branches arising from the anterior Glissonian pedicle should be exposed and divided. According to previous reports, stepwise logistic regression analysis identified a surgical procedure in which the cut surface exposed the major Glissonean pedicle to be an independent predictor of postoperative bile leakage [14]. Therefore, careful attention and meticulous manipulation are required to prevent bile leakage from the main anterior trunk, as this is one of the almost incurable postoperative complications of hepatic resection.

The current study did not include the long-term outcome of the patients who underwent THR-RHV. As metastasis of hepatocellular carcinoma via the portal vein is important, an anatomical hepatic resection according to the portal vein is recommended to prevent recurrence after the resection [21]. For this reason, conventional right hepatic lobectomy should be performed if the RmLV is sufficient. Conversely, THR-RHV is recommended if the tumor is located close to the RHV without sufficient remnant volume. Tanaka et al. [18] reported favorable long-term results in 11 patients following venous limited resection of the right hemiliver, guided by the area of hepatic venous drainage. Further studies on a large number of patients should be undertaken to assess the oncological effects of this procedure.

In conclusion, THR-RHV was proved to be a feasible and effective treatment modality with acceptable perioperative results. By using this technique, the safety and curability of surgery for patients with tumors close to the RHV can be expected to improve.

Acknowledgments We thank Professor Brian Quinn for his review of the manuscript. We are also grateful to Mr. Leon Sakuma for his excellent help in preparing the figures. This study was supported in part by a grant from the Scientific Research Fund of the Ministry of Education of Japan.

Conflict of interest All of the authors report no conflicts of interest.

References

1. Taketomi A, Kitagawa D, Itoh S, Harimoto N, Yamashita Y, Gion T, et al. Trends in morbidity and mortality after hepatic resection for hepatocellular carcinoma: an institute's experience with 625 patients. J Am Coll Surg. 2007;204:580–7.
2. Hasegawa K, Kokudo N. Surgical treatment of hepatocellular carcinoma. Surg Today. 2009;39:833–43.
3. Shirabe K, Shimada M, Gion T, Hasegawa H, Takenaka K, Utsunomiya T, et al. Postoperative liver failure after major hepatic resection for hepatocellular carcinoma in the modern era with special reference to remnant liver volume. J Am Coll Surg. 1999;188:304–9.
4. Hemming AW, Reed AI, Howard RJ, Fujita S, Hochwald SN, Caridi JG, et al. Preoperative portal vein embolization for extended hepatectomy. Ann Surg. 2003;237:686–91.
5. Nakamura S, Sakaguchi S, Hachiya T, Suzuki S, Nishiyama R, Konno H, et al. Significance of hepatic vein reconstruction in hepatectomy. Surgery. 1993;114:59–64.
6. Narita M, Oussoultzoglou E, Chenard MP, Rosso E, Casnedi S, Pessaux P, et al. Sinusoidal obstruction syndrome compromises liver regeneration in patients undergoing two-stage hepatectomy with portal vein embolization. Surg Today. 2011;41:7–17.
7. Cho A, Okazumi S, Makino H, Miura F, Shuto K, Mochiduki R, et al. Anterior fissure of the right liver—the third door of the liver. J Hepatobiliary Pancreat Surg. 2004;11:390–6.
8. Cho A, Okazumi S, Makino H, Miura F, Ohira G, Yoshinaga Y, et al. Relation between hepatic and portal veins in the right paramedian sector: proposal for anatomical reclassification of the liver. World J Surg. 2004;28:8–12.
9. Ryu M, Cho A. New liver anatomy: portal segmentation and the drainage vein. Berlin: Springer; 2009.
10. Kondo S, Katoh H, Hirano S, Ambo Y, Tanaka E, Saito K, et al. Venous-drainage-guided selective hepatectomy: a novel approach to liver surgery. Hepatogastroenterology. 2004;51:1–3.
11. Yonemura Y, Taketomi A, Soejima Y, Yoshizumi T, Uchiyama H, Gion T, et al. Validity of preoperative volumetric analysis of congestion volume in living donor liver transplantation using three-dimensional computed tomography. Liver Transpl. 2005;11:1556–62.
12. Kayashima H, Taketomi A, Yonemura Y, Ijichi H, Harada N, Yoshizumi T, et al. Accuracy of an age-adjusted formula in assessing the graft volume in living donor liver transplantation. Liver Transpl. 2008;14:1366–71.
13. Sano K, Makuuchi M, Takayama T, Sugawara Y, Imamura H, Kawarasaki H. Technical dilemma in living-donor or split-liver transplant. Hepatogastroenterology. 2000;47:1208–9.
14. Yamashita Y, Hamatsu T, Rikimaru T, Tanaka S, Shirabe K, Shimada M, et al. Bile leakage after hepatic resection. Ann Surg. 2001;233:45–50.
15. Saito S, Yamanaka J, Miura K, Nakao N, Nagao T, Sugimoto T, et al. A novel 3D hepatectomy simulation based on liver circulation: application to liver resection and transplantation. Hepatology. 2005;41:1297–304.
16. Fukuhara T, Umeda K, Toshima T, Takeishi K, Morita K, Nagata S, et al. Congestion of the donor remnant right liver after extended left lobe donation. Transpl Int. 2009;22:837–44.
17. Taketomi A, Kayashima H, Soejima Y, Yoshizumi T, Uchiyama H, Ikegami T, et al. Donor risk in adult-to-adult living donor liver transplantation: impact of left lobe graft. Transplantation. 2009;87:445–50.
18. Tanaka K, Matsumoto C, Takakura H, Matsuo K, Nagano Y, Endo I, et al. Technique of right hemihepatectomy preserving ventral right anterior section guided by area of hepatic venous drainage. Surgery. 2010;147:450–8.
19. Kaneko J, Sugawara Y, Sato S, Kishi Y, Akamatsu N, Togashi J, et al. Relation between the middle hepatic vein drainage area volume and alanine aminotransferase after left liver harvesting. Transplant Proc. 2005;37:2166–8.
20. Kido M, Ku Y, Fukumoto T, Tominaga M, Iwasaki T, Ogata S, et al. Significant role of middle hepatic vein in remnant liver regeneration of right-lobe living donors. Transplantation. 2003;75:1598–600.
21. Yamashita Y, Taketomi A, Itoh S, Kitagawa D, Kayashima H, Harimoto N, et al. Longterm favorable results of limited hepatic resections for patients with hepatocellular carcinoma: 20 years of experience. J Am Coll Surg. 2007;205:19–26.

Hepatology Research

Hepatology Research 2012; **42**: 288–295 doi: 10.1111/j.1872-034X.2011.00927.x

Original Article

Efficacy of splenectomy in preventing anemia in patients with recurrent hepatitis C following liver transplantation is not dependent on inosine triphosphate pyrophosphatase genotype

Takashi Motomura, Erina Koga, Akinobu Taketomi, Takasuke Fukuhara, Yohei Mano, Jun Muto, Hideyuki Konishi, Takeo Toshima, Hideaki Uchiyama, Tomoharu Yoshizumi, Ken Shirabe and Yoshihiko Maehara

Department of Surgery and Science, Graduate School of Medical Sciences, Kyushu University, Fukuoka, Japan

Aim: A genetic polymorphism of inosine triphosphate pyrophosphatase (ITPA) has been associated with pegylated-interferon/ribavirin (PEG-IFN/RBV)-induced anemia in chronic hepatitis C patients. However, correlation of the genetic variant with anemia following liver transplantation has not been determined.

Methods: Sixty-three hepatitis C virus (HCV)-positive patients who underwent liver transplantation and PEG-IFN/RBV therapy were enrolled. The rs1127354 was determined for each individual.

Results: There was no relationship with anemia or RBV dosage in patients carrying the CC allele (CC group, $n = 43$) and those carrying the CA allele (CA group, $n = 20$). The incidence of hemoglobin (Hb) decline >3 g/dL (CC: 4.7%, CA: 0%) was relatively low, whereas the incidence of Hb levels <10 g/dL (CC: 18.6%, CA: 30.0%) was high. Univariate analysis revealed that splenectomy inversely correlated with Hb levels <10 g/dL at 4 weeks ($P = 0.04$). Among the 22 patients who did not undergo splenectomy, the incidence of Hb levels <10 g/dL tended to be lower in the seven patients carrying the CA allele (28.6%) than in the 15 patients with the CC allele (60.0%).

Conclusion: The ITPA genetic polymorphism does not correlate with post-transplant PEG-IFN/RBV-induced anemia. Splenectomy is useful in preventing anemia regardless of the ITPA genotype.

Key words: inosine triphosphate pyrophosphatase genetic polymorphism, liver transplantation, recurrent hepatitis C, splenectomy

INTRODUCTION

HEPATITIS C VIRUS (HCV) and its related diseases are the leading cause of liver transplantation (LT) worldwide.[1] The incidence of HCV re-infection is increased in almost all cases after LT and the outcome of post-transplant antiviral therapy is very poor.[2] Although the combination of pegylated interferon and ribavirin (PEG-IFN/RBV) is the standard antiviral therapy for HCV, it is expensive and has some side effects such as flu-like symptoms, thrombocytopenia, and anemia. Of these problems, anemia is a serious matter, especially for Japanese patients, as erythropoietin replacement therapies are not covered by public medical insurance and are seldom performed. Furthermore, the incidence of anemia after LT is as high as 50%, even without anti-HCV therapy.[3] PEG-IFN/RBV therapy for recurrent hepatitis C after LT has been reported to cause anemia in no less than 71% of recipients.[4] To prevent these side effects, various techniques have been trialed, including: (i) simultaneous splenectomy at transplantation,[5] and (ii) PEG-IFN-α2 therapy with 200 mg RBV daily followed by an increase in dosage according to the tolerance of the individual.[6]

Recently, two single nucleotide polymorphisms (SNPs) in the inosine triphosphatase pyrophosphatase

Correspondence: Dr Akinobu Taketomi, Department of Surgery and Science, Graduate School of Medical Sciences, Kyushu University, Fukuoka 812-8582, Japan. Email: taketomi@surg2.med.kyushu-u.ac.jp

Conflict of interest: There are no competing interests regards to this work.

Received 30 August 2011; revision 28 September 2011; accepted 12 October 2011.

(ITPA) gene were reported to correlate with treatment-induced anemia in chronic hepatitis C patients. These were identified as rs1127354 and rs7270101.[7] These two SNPs are known to be responsible for ITPA deficiency[7] and inosine triphosphate (ITP) accumulation in erythrocytes, and are thought to confer protective effects in ribavirin-related hemolytic anemia. Of these two SNPs, rs7270101 is not polymorphic in Japanese people,[8] but variants at rs1127354 have been demonstrated to be significantly associated with treatment-induced anemia in Japanese hepatitis C patients.[9,10]

If this genetic polymorphism is a predictor of anemia after post-transplant PEG-IFN/RBV therapy, then that would lead to a new tailored anti-HCV treatment post-LT. In this article, we describe the relationship of the ITPA genetic polymorphism to anemia in LT patients undergoing PEG-IFN/RBV therapy, and demonstrate the usefulness of our strategies against the aforementioned side effects.

METHODS

Patients

FROM APRIL 1999 to March 2009, 112 HCV-RNA-positive patients underwent LT at our institute, of which 78 patients were administered PEG-IFN/RBV therapy. Of these 78 patients, five patients who were under treatment, six patients who dropped out from treatment because of its side effect other than anemia such as depression, and three patients whose Hb levels after treatment were unavailable, were excluded from this study. Therefore, 63 patients were retrospectively analyzed. The current study was approved by the ethics committee of Kyushu University.

Antiviral treatment

The primary doses of PEG-IFN α2b (Pegintron®; Schering-Plough Inc, Kenilworth, NJ, USA) and RBV (Rebetol®; Schering-Plough Inc) were 0.5 μg/kg per week and 200 mg daily, respectively. They were increased to 1.5 μg/kg per week and 800 mg daily in a stepwise manner according to individual tolerance as previously described.[6] Neither granulocyte colony-stimulating factor nor erythropoietin was used in any individual.

Assessment of the therapeutic effects and anemia

A virological response (VR) was defined as a lack of HCV RNA in response to the treatment regimen regardless of whether a relapse occurred when treatment was terminated. A sustained virological response (SVR) was defined as a lack of HCV RNA at 6 months after completion of the treatment. Treatment-induced anemia was defined as a decline in hemoglobin (Hb) greater than 3 g/dL at 4 weeks, or a Hb level less than 10 g/dL at 4 weeks as previously described.[7]

DNA extraction and ITPA genotyping

DNA was extracted from the recipient's exenterated liver tissue at transplantation, and direct sequencing was performed using a Big Dye Terminator v1.1 Cycle Sequence Kit (Applied Biosystems Inc., Tokyo, Japan) according to the manufacturer's protocol. The primers used to identify the ITPA genetic polymorphism (rs1127354) were 5′-AGA GTT ATC GAT GAG AAA-3′ (sense) and 5′-GAG AAA TCC AAC CAT CTT-3′ (antisense).

Statistical analysis

All data was analyzed using JMP® statistical software. A χ^2 test was performed for qualitative variables and a Wilcoxon test was performed for quantitative variables.

RESULTS

ITPA genotyping and anemia

THE ITPA MAJOR homozygote allele (rs1127354: CC) was seen in 43 recipients (68.3%) and the heterozygote allele (CA) was seen in 20 recipients (31.7%). No recipient enrolled in the current study carried the minor homozygote allele (AA). The patients' backgrounds between these two genotypes have been outlined in Table 1. None of the pre-transplant, operative, and pre-treatment factors exhibited any differences, except for pre-treatment viral titre.

Among those carrying the CC allele, only two recipients (4.7%) showed a decline in Hb greater than 3 g/dL at 4 weeks after the commencement of PEG-IFN/RBV therapy; whereas none of the recipients carrying the CA allele showed a Hb decline greater than 3 g/dL ($P = 0.311$; Fig. 1a). In contrast, eight recipients whose Hb level was less than 10 g/dL at 4 weeks carried the CC allele and six carried the CA allele ($P = 0.327$; Fig. 1b). In addition, the progression of anemia during the treatment between two groups were compared by each Hb decline at 4, 8, and 12 weeks after commencement of the therapy to reveal that there was no difference (−0.92 g/dL vs. −0.59 g/dL; $P = 0.59$, −1.33 g/dL vs. −0.74 g/dL; $P = 0.27$, −1.39 g/dL vs.